Short-Term Prediction of a Nocturnal Significant Tornado Outbreak Using a Convection-Allowing Ensemble

THOMAS J. GALARNEAU JR.,[a,b] LOUIS J. WICKER,[b] KENT H. KNOPFMEIER,[a,b] WILLIAM J. S. MILLER,[c,d] PATRICK S. SKINNER,[a,b] AND KATIE A. WILSON[a,b]

[a] *Cooperative Institute for Severe and High-Impact Weather Research and Operations, University of Oklahoma, Norman, Oklahoma*
[b] *NOAA/OAR/National Severe Storms Laboratory, Norman, Oklahoma*
[c] *Cooperative Institute for Satellite Earth System Studies, Earth System Science Interdisciplinary Center, University of Maryland, College Park, College Park, Maryland*
[d] *NOAA/NESDIS/Center for Satellite Applications and Research, College Park, Maryland*

(Manuscript received 28 September 2021, in final form 18 February 2022)

ABSTRACT: A multiscale analysis of the significant nocturnal tornado outbreak in Tennessee on 2–3 March 2020 is presented. This outbreak included several significant tornadoes and resulted in the second most fatalities (25) and most injuries (309) of all nocturnal tornado events in Tennessee in 1950–2020. The two deadliest tornadoes struck Nashville (EF3 intensity) and Cookeville (EF4) resulting in 5 and 19 fatalities, respectively. The supercell responsible for the tornado outbreak initiated at 0330 UTC 3 March within a region of warm frontogenesis in western Tennessee. Throughout its life cycle, the supercell was located in a region of convective available potential energy near 1000 J kg^{-1} and 0–1-km storm-relative helicity over 350 m^2 s^{-2}. Retrospective 3-h forecasts from the experimental Warn-on-Forecast System (WoFS) convection-allowing ensemble initialized after the parent supercell initiated indicated a high probability, high severity scenario for tornadoes across Tennessee and into Nashville through 0700 UTC. Earlier WoFS forecasts indicated a low probability, high severity scenario owing to uncertainty in the initiation of supercells. The presence of these supercells was sensitive to the upstream thermodynamic conditions and warm frontogenesis regions that were inherited from the lateral boundary conditions. In all, this study highlights the potential of the WoFS ensemble to contribute useful probabilistic severe weather information to the short-term forecast process during a nocturnal significant tornado outbreak.

KEYWORDS: Severe storms; Tornadoes; Numerical weather prediction/forecasting; Short-range prediction; Ensembles

1. Introduction

A nocturnal tornado outbreak occurred on 2–3 March 2020 in the Tennessee and lower Ohio Valleys, concentrated across northern Tennessee at 0300–0900 UTC 3 March. Of the 13 tornadoes that occurred in Tennessee, 6 were significant with an EF2 or higher rating on the enhanced Fujita scale (WSEC 2006; Fujita 1981). Three of the significant tornadoes resulted in fatalities. The first deadly tornado (rated EF2) began at 0505 UTC 3 March in Benton County, Tennessee, resulting in 1 fatality and 2 injuries (Fig. 1). The second deadly tornado (EF3) began at 0632 UTC and moved through the northern portion of the Nashville, Tennessee, metropolitan area resulting in 5 fatalities and 220 injuries. The third deadly tornado (EF4) began at 0748 UTC and resulted in 19 fatalities and 87 injuries as it moved through Cookeville, Tennessee. In addition to an outbreak of tornadoes, numerous severe thunderstorm wind, hail, and flash flood reports occurred in Missouri and extended east of the Mississippi River into Kentucky and Tennessee.

Day 1 tornado probability outlooks issued by the Storm Prediction Center (SPC) earlier on 2 March and at 0100 UTC 3 March consistently included the Nashville, Tennessee, area in a 2% tornado probability region. A 5% tornado probability region was centered farther west near the Mississippi River. It was expected that supercells near the Mississippi River would grow upscale into a mesoscale convective system (MCS) and have the potential to produce damaging winds and hail farther east in the Tennessee Valley. The National Weather Service in Nashville (OHX) generated a forecast graphic at 1756 UTC 2 March that showed severe storms with all hazards were possible in the Nashville area in the 0600–1100 UTC 3 March time frame (Fig. 2 in Ellis et al. 2020). The Nashville tornado parent supercell initiated at 0330 UTC in western Tennessee and produced its first tornado (EF1) at 0410 UTC (Fig. 1). In response to the development and eastward progression of this tornadic supercell, the SPC issued a tornado watch for the Nashville area at 0520 UTC. Tornado warnings were issued by OHX at 0513 and 0540 UTC for the supercell when it was located in counties west of Nashville. Both SPC and OHX recognized the increasing tornado threat with the parent supercell by issuing a tornado watch and the first tornado warnings 70–80 min prior to the supercell reaching Nashville. A severe thunderstorm warning that included Nashville was issued at 0611 UTC and the first tornado warning for Nashville was issued at 0635 UTC, approximately 8–10 min prior to the EF3 tornado impacting the metropolitan area.

Given how this case represents a nocturnal significant tornado outbreak that included numerous fatalities and impacted a metropolitan area, it is of interest to use available observations and numerical model analyses to document the life cycle of the parent supercell and the mesoscale environment in

Corresponding author: Thomas J. Galarneau Jr., thomas.galarneau@noaa.gov

DOI: 10.1175/WAF-D-21-0160.1

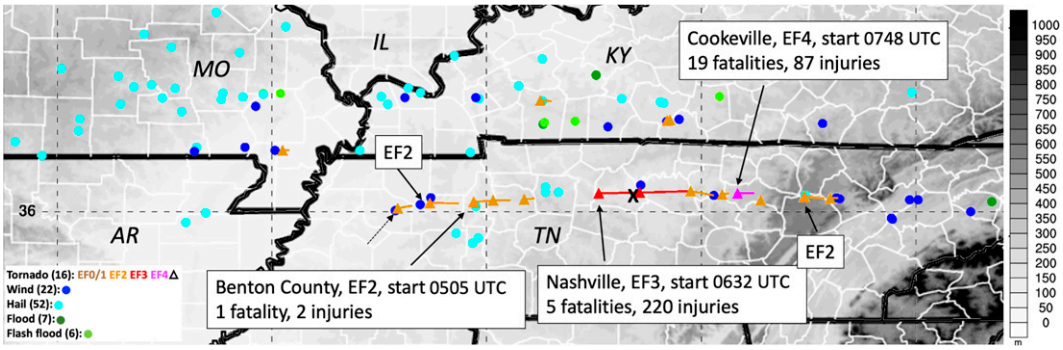

FIG. 1. NOAA/NCEI *Storm Data* tornado, wind, hail, flash flood, and flood reports (symbols and colors according to the key) for 2300 UTC 2 Mar–1400 UTC 3 Mar 2020 overlaid on NOAA/NCEI ETOPO1 1-arc-min global relief model (Amante and Eakins 2009) terrain height (shaded according to the grayscale; m). Tornadoes with damage rating EF2+ are labeled and include number of fatalities and injuries when applicable. The tornado track is marked by a line segment colored according to the key, with a triangle marking the starting location. Nashville, TN, is marked with an "X." The first tornado produced by the parent supercell is marked by the black dashed arrow.

which it occurred. Furthermore, we will examine short-term forecasts from an experimental convection-allowing ensemble prediction system and illustrate how uncertainty in the upstream mesoscale environment in Arkansas impacted the convection forecast in Tennessee.

a. Background

Severe weather events in the eastern United States are frequently associated with quasi-linear convective systems (QLCSs), with 30%–42% of severe reports associated with QLCSs in the Ohio and Mississippi Valleys (Ashley et al. 2019). While 21% of all tornado reports in these regions are associated with QLCSs (Ashley et al. 2019), most significant tornadoes in the Tennessee and Ohio Valleys are associated with supercells (Smith et al. 2008). The nocturnal tornado outbreak on 2–3 March 2020 occurred in conjunction with a long-lived supercell that was isolated initially and later became embedded in the southern edge of the QLCS to the north. This event occurred at the tail end of the cool season in a region (western and central Tennessee) where cool season tornadoes are increasing more than anywhere else in the United States in the 63-yr period 1953–2015 (Childs et al. 2018). Nocturnal tornadoes are common occurrences in the southeast United States, including the Mississippi and Ohio Valley region where over a third of tornadoes are nocturnal (Fig. 6 in Ashley et al. 2008). Tennessee has the highest fraction of nocturnal tornadoes (~45%) in the United States. While the predictability of nocturnal tornadoes in the southeast United States is similar to other regions and times of day (Bunker et al. 2019), these tornadoes are more likely to result in fatalities with most of these fatalities occurring in mobile homes (Ashley et al. 2008). Kis and Straka (2010) identified 70 nocturnal tornadoes in 2014–16 and found that 88% were associated with QLCSs and 10% with isolated supercells. All but one of the tornadoes associated with isolated supercells occurred in the Plains, which highlights the relative rarity of the isolated supercell in Tennessee on 2–3 March.

The environments in which nocturnal tornado events occur are typically characterized by low values of instability, with convective available potential energy (CAPE) values below 1000 J kg^{-1}, and high values of vertical wind shear. These high shear, low CAPE (HSLC) tornado events occur most commonly in the Mississippi Valley region (Sherburn and Parker 2014). While the occurrence of these events can be

TABLE 1. The top 10 tornado days in Tennessee for 1950–2020 ranked according to adjusted Fujita miles (AFMs). The day listed defines the beginning of the 24-h period at 1200 UTC. Other characteristics of the tornado days are the count of all tornadoes, significant tornadoes (rated ≥F/EF2), violent tornadoes (rated ≥F/EF4), direct fatalities, and direct injuries. The Nashville tornado outbreak is highlighted in bold font.

Rank	Day	AFMs	No. of tornadoes	Significant tornadoes	Violent tornadoes	Fatalities	Injuries
1	3 Apr 1974	960.1	51	33	10	45	749
2	27 Apr 2011	631.5	77	23	7	31	425
3	16 Apr 1998	463.8	19	15	3	5	105
4	5 Feb 2008	370.9	37	15	2	31	148
5	4 May 2003	352.7	24	8	2	11	100
6	21 Mar 1952	322.2	13	13	6	67	294
7	**2 Mar 2020**	**253.9**	**13**	**6**	**1**	**25**	**309**
8	23 Dec 2015	224.4	12	6	2	2	7
9	7 May 1971	204.7	5	3	3	3	137
10	18 May 1995	182.7	23	4	1	3	86

TABLE 2. As in Table 1, but for the overnight period defined as 0300–1200 UTC. The day listed defines the beginning of the 24-h period at 1200 UTC. For example, the Nashville tornado outbreak began after 0300 UTC 3 Mar, but occurred within the 24-h period that began at 1200 UTC 2 Mar. The Nashville tornado outbreak is highlighted in bold font.

Rank	Day	AFMs	No. of tornadoes	Significant tornadoes	Violent tornadoes	Fatalities	Injuries
1	4 May 2003	331.7	19	7	2	11	100
2	**2 Mar 2020**	**253.9**	**13**	**6**	**1**	**25**	**309**
3	21 Mar 1952	248.3	10	10	4	51	249
4	3 Apr 1974	163.2	15	6	0	5	204
5	1 May 2010	115.6	16	7	0	1	15
6	23 Apr 1970	104.9	4	4	0	0	24
7	5 Nov 2018	93.8	16	4	0	1	3
8	5 Feb 2008	87.7	10	3	0	22	63
9	3 Apr 1968	79.8	3	2	0	4	32
10	13 Feb 1952	79.8	5	4	2	3	48

linked to remote influences such as the sea surface temperature in the Gulf of Mexico (e.g., Molina et al. 2018), key discriminators for HSLC tornado events are high values of vertical wind shear and lapse rates at low levels (Sherburn and Parker 2014, 2019). These HSLC environments are frequently found in a moist warm sector of a surface low pressure system and along cold fronts (Sherburn et al. 2016). Kis and Straka (2010) note that substantial low-level vertical wind shear and storm-relative helicity (SRH), strong low-level jets, and marginal instability are most often associated with nocturnal significant tornadoes. Coffer et al. (2019) further suggest that SRH in the lowest few hundred meters above the ground may be a better indicator for higher tornado probabilities than vertical wind shear and SRH in deeper layers (e.g., 0–3 km).

b. Science objectives

The Nashville tornado represents an illustrative example of the hazards and forecaster challenges associated with a nocturnal significant tornado impacting a metropolitan area (Ellis et al. 2020). These challenges include communicating the tornado risk before dark, the public receiving the warnings while asleep, and an inability to obtain real-time storm reports as the event unfolds. The latter challenge can further complicate the issuance of tornado warnings, making it difficult to assess tornado risk using mesocyclone signatures on radar alone. From a historical perspective of tornado events in Tennessee, the 2–3 March 2020 event ranked 7th among the top 10 tornado days (24-h period ending 1200 UTC) in Tennessee for 1950–2020 ranked according to adjusted Fujita miles (AFMs; as defined by Fuhrmann et al. 2014) and resulted in the fifth most fatalities and third most injuries (Table 1). When considering tornadoes that occur during the overnight period 0300–1200 UTC only, 2–3 March 2020 ranks second in AFMs and fatalities and first in injuries (Table 2). The historical significance, socioeconomic impact of, and forecast challenges posed by this nocturnal tornado outbreak motivates the need for detailed analysis and diagnosis of this event.

This paper aims to improve understanding of this event by addressing the following science questions: 1) What synoptic- and mesoscale features contributed to environmental ingredients favorable for a long-lived tornadic supercell in Tennessee? 2) Can an experimental convection-allowing ensemble prediction system add value to the short-term forecast process and show the potential to extend the watch and warning lead time for nocturnal tornadoes like those that occurred on 2–3 March 2020? The convection-allowing ensemble Warn-on-Forecast System (WoFS; Wheatley et al. 2015; Jones et al. 2016) will be used to address the second science question.

c. Organization

The remainder of this paper is organized as follows. Section 2 describes the observational and model datasets used for the synoptic- and mesoscale analysis and introduces the WoFS. Section 3 presents an overview of the parent supercell life cycle. Section 4 presents a synoptic analysis and an examination of the mesoscale environment. An analysis and diagnosis of the WoFS short-term predictions of the Nashville tornadic supercell is presented in section 5. Section 6 provides the conclusions.

2. Data and methods

The analysis presented herein was constructed using several observational and modeling datasets. The storm reports were obtained from the National Oceanic and Atmospheric Administration (NOAA)/National Centers for Environmental Information (NCEI) Storm Events Database version 3.1 (NOAA 2021). The Automated Surface Observing System (ASOS) observations were obtained from NOAA/NCEI and observed soundings of temperature, dewpoint, and wind from the Iowa State University Environmental Mesonet data archive. The Multi-Radar Multi-Sensor (MRMS) 1 km above ground level (AGL) reflectivity and 0–2-km azimuthal shear (Lakshmanan et al. 2007; Smith et al. 2016) were used to examine the life cycle of the parent supercell responsible for the nocturnal tornado outbreak. The synoptic-scale environment was determined using the National Centers for Environmental Prediction (NCEP) Global Forecast System (GFS) analysis pressure-level data available at 6-h intervals at 0.25° × 0.25° latitude–longitude grid spacing. The mesoscale environment was determined using the operational version of the NCEP High Resolution Rapid Refresh (HRRR) version 3 analyses

TABLE 3. Summary of boundary conditions, physical parameterizations, and UH_m ($m^2 s^{-2}$) for WoFS forecast members initialized at 2300 UTC 2 Mar and 0000 UTC 3 Mar 2020. The forecast metric, UH_m, is described later in section 5b. Members with the top 10 UH_m are in bold text, and bottom 10 UH_m are in italics. The PBL options include the Yonsei University (YSU), Mellor–Yamada–Janjić (MYJ), and Mellor–Yamada–Nakanashi–Niino (MYNN) parameterizations, and are combined with the Dudhia (1989) and Rapid Radiative Transfer Model (RRTM) or the Rapid Radiative Transfer Model for GCMs (RRTMG) radiation physics options. The physical parameterization options are adapted from Skinner et al. (2018, their Table 1).

Initial time	WoFS member	HRRRE BC Mem	WoFS PBL	Shortwave radiation	Longwave radiation	UH_m ($m^2 s^{-2}$)	Rank
2300	**1**	**1**	**YSU**	**Dudhia**	**RRTM**	**10.4**	**2**
2300	2	2	YSU	RRTMG	RRTMG	4.2	19
2300	*3*	*3*	*MYJ*	*Dudhia*	*RRTM*	*0.1*	*35*
2300	**4**	**4**	**MYJ**	**RRTMG**	**RRTMG**	**7.6**	**8**
2300	*5*	*5*	*MYNN*	*Dudhia*	*RRTM*	*2.3*	*29*
2300	**6**	**6**	**MYNN**	**RRTMG**	**RRTMG**	**9.1**	**3**
2300	7	7	YSU	Dudhia	RRTM	5.7	15
2300	**8**	**8**	**YSU**	**RRTMG**	**RRTMG**	**8.5**	**5**
2300	**9**	**9**	**MYJ**	**Dudhia**	**RRTM**	**8.6**	**4**
2300	**10**	**1**	**MYJ**	**RRTMG**	**RRTMG**	**10.9**	**1**
2300	*11*	*2*	*MYNN*	*Dudhia*	*RRTM*	*1.5*	*32*
2300	12	3	MYNN	RRTMG	RRTMG	3.5	22
2300	13	4	YSU	Dudhia	RRTM	3.4	24
2300	14	5	YSU	RRTMG	RRTMG	3.9	21
2300	15	6	MYJ	Dudhia	RRTM	5.7	14
2300	16	7	MYJ	RRTMG	RRTMG	3.1	26
2300	*17*	*8*	*MYNN*	*Dudhia*	*RRTM*	*1.6*	*31*
2300	**18**	**9**	**MYNN**	**RRTMG**	**RRTMG**	**7.0**	**10**
0000	**1**	**1**	**YSU**	**Dudhia**	**RRTM**	**8.5**	**6**
0000	*2*	*2*	*YSU*	*RRTMG*	*RRTMG*	*3.0*	*27*
0000	*3*	*3*	*MYJ*	*Dudhia*	*RRTM*	*0.4*	*34*
0000	**4**	**4**	**MYJ**	**RRTMG**	**RRTMG**	**7.1**	**9**
0000	*5*	*5*	*MYNN*	*Dudhia*	*RRTM*	*2.4*	*28*
0000	6	6	MYNN	RRTMG	RRTMG	4.1	20
0000	7	7	YSU	Dudhia	RRTM	5.3	17
0000	8	8	YSU	RRTMG	RRTMG	6.2	12
0000	9	9	MYJ	Dudhia	RRTM	6.3	11
0000	**10**	**1**	**MYJ**	**RRTMG**	**RRTMG**	**8.3**	**7**
0000	*11*	*2*	*MYNN*	*Dudhia*	*RRTM*	*0.0*	*36*
0000	*12*	*3*	*MYNN*	*RRTMG*	*RRTMG*	*1.8*	*30*
0000	13	4	YSU	Dudhia	RRTM	3.3	25
0000	14	5	YSU	RRTMG	RRTMG	5.4	16
0000	15	6	MYJ	Dudhia	RRTM	4.4	18
0000	16	7	MYJ	RRTMG	RRTMG	3.5	23
0000	*17*	*8*	*MYNN*	*Dudhia*	*RRTM*	*1.1*	*33*
0000	18	9	MYNN	RRTMG	RRTMG	6.0	13

available hourly at 3-km horizontal grid spacing. The Miller (1948) frontogenesis equation was used to examine the role of frontogenesis by the horizontal wind in driving mesoscale ascent in the pre-storm environment, and is defined as

$$F = \frac{1}{|\nabla\theta|}\left[-\frac{\partial\theta}{\partial x}\left(\frac{\partial u}{\partial x}\frac{\partial\theta}{\partial x}+\frac{\partial v}{\partial x}\frac{\partial\theta}{\partial y}\right)-\frac{\partial\theta}{\partial y}\left(\frac{\partial u}{\partial y}\frac{\partial\theta}{\partial x}+\frac{\partial v}{\partial y}\frac{\partial\theta}{\partial y}\right)\right], \quad (1)$$

where F is the frontogenesis, ∇ is the gradient operator on a pressure surface, θ is potential temperature, u is the zonal wind component, and v is the meridional wind component. In (1), frontogenesis is driven by horizontal shear and confluence of the horizontal wind and effects from tilting and diabatic heating are not included.

The NOAA National Severe Storms Laboratory (NSSL) WoFS is an ensemble forecast system based on the Advanced Research version of the Weather Research and Forecasting (ARW; Skamarock et al. 2008) Model, version 3.9.1. The 36-member WoFS data assimilation system is cycled every 15 min beginning with the High-Resolution Rapid Refresh Ensemble (HRRRE; Dowell et al. 2016) at 1200 UTC 2 March 2020. In addition to assimilating conventional observations, Oklahoma Mesonet, geostationary satellite, and three-dimensional MRMS reflectivity and radial velocity observations (14 vertical levels below 10 km AGL) are assimilated. The details of the data assimilation cycling are summarized most recently by Yussouf et al. (2020, their section 2a). At each hour from 2000 UTC 2 March to 0600 UTC 3 March, 3-h forecasts are initialized for the first 18 members of the WoFS ensemble. It is these forecasts that will be presented in section 5 to examine short-term prediction of the nocturnal tornado outbreak.

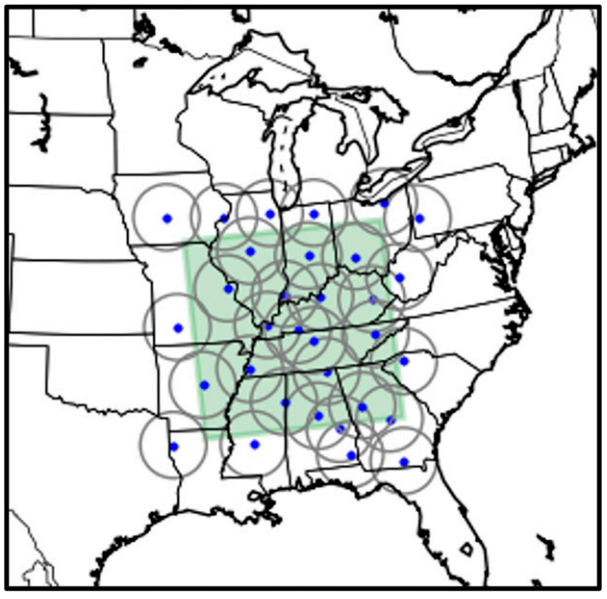

FIG. 2. WoFS model domain (green region) and WSR-88Ds (blue filled diamond within unfilled gray circle) used in the data assimilation cycling.

The WoFS configuration is summarized in Table 3 and described below. The WoFS is run using 51 vertical levels to 10 hPa and at a convection-allowing (no cumulus parameterization) 3-km horizontal grid spacing on a 900 km × 900 km domain (Fig. 2). The NSSL two-moment microphysics (Mansell et al. 2010) and Rapid Update Cycle land surface model (Smirnova et al. 2016) are implemented among all ensemble members. The 9-member HRRRE forecast initialized at 1200 UTC 2 March is used as the lateral boundary conditions. In addition to varying the boundary conditions among the ensemble members, different combinations of the planetary boundary layer (PBL) and radiation physics parameterizations are used. The PBL physics include the Yonsei University (YSU; Hong et al. 2006), Mellor–Yamada–Janjić (MYJ; Mellor and Yamada 1982; Janjić 2002), and Mellor–Yamada–Nakanishi–Niino (MYNN; Nakanishi and Niino 2004, 2006) parameterizations. The radiation physics include a combination of the Dudhia (1989) shortwave and Rapid Radiative Transfer Model (RRTM) longwave radiation or the Rapid Radiative Transfer Model for GCMs (RRTMG) for longwave and shortwave radiation.

3. Life cycle of the long-lived supercell in Tennessee

A region of scattered showers developed by 0300 UTC in western Tennessee just east of the Mississippi River (Fig. 3a). The parent supercell for the nocturnal tornado outbreak originated from the southernmost showers in this region and quickly developed low-level rotation based on the accumulated 0–2-km azimuthal shear by 0400 UTC (Fig. 3b). The azimuthal shear increased through 0540 UTC as the isolated supercell produced five tornadoes, including two at EF2 intensity, which resulted in one fatality (Figs. 1 and 3c). By 0600 UTC, the supercell was located west of Nashville in Dickson County, Tennessee and was evolving to a supercell embedded on the southern edge of the QLCS in Kentucky and northern Tennessee (Fig. 3d). A well-defined low-level rotation track was evident along the path of the supercell north of Interstate-40. Low-level rotation temporarily weakened from 0600 to 0620 UTC, and then rapidly increased through 0630 UTC in concert with development of the EF3 tornado that moved through Nashville thereafter (Figs. 1 and 3e).

By 0700 UTC, the tornadic supercell was located just east of Nashville (Fig. 3e). As the Nashville EF3 tornado dissipated, the supercell produced another tornado (EF1) at 0715 UTC that lasted through 0730 UTC. The supercell continued east along Interstate-40 through 0800 UTC where it produced EF0 tornadoes east of Gordonsville at 0738 UTC and near Goffton, Tennessee, at 0805 UTC (Figs. 1 and 3f). Between the times of these tornadoes, the supercell produced an EF4 tornado from 0748 to 0756 UTC that resulted in 19 fatalities in Cookeville, Tennessee. Detailed examination of the KOHX base reflectivity and radial velocity reveals that as the mesocyclone that produced the Nashville tornado dissipated by 0724 UTC, a new mesocyclone formed to its south and became the primary circulation that moved to the north side of Cookeville by 0756 UTC while producing an EF4 tornado (not shown). A third mesocyclone formed southwest of the Cookeville mesocyclone at 0746 UTC, moved south of Cookeville and produced the EF0 tornado in Goffton after 0800 UTC. Following the Cookeville and Goffton tornadoes, the supercell continued eastward and produced an EF2 tornado at 0825 UTC in Cumberland County and an EF0 at 0840 UTC in Morgan County before dissipating.

4. Synoptic and mesoscale analysis

The aim of this section is to examine the synoptic and mesoscale environment in which the nocturnal tornado outbreak in Tennessee occurred. For analysis of the mesoscale environment, an emphasis will be placed on the time period from supercell initiation through the time of the Nashville EF3 tornado.

a. Synoptic-scale flow

The synoptic-scale flow pattern at 1800 UTC 2 March 2020 was characterized by a positively tilted trough at 250 hPa extending from the Great Lakes region to the southwest United States (Fig. 4a). Broad southwesterly flow at 850 hPa extended from the southern Plains through the Tennessee Valley on the eastern flank of a surface trough (Fig. 4b). By 0000 UTC 3 March, a potential vorticity (PV) maximum embedded in the positively tilted trough at 250 hPa moved east to central Kansas (Fig. 4c). The 250-hPa wind increased to over 80 m s^{-1} from Oklahoma to Tennessee in conjunction with a strengthening upper-level PV gradient due to negative advection of PV by the divergent wind on the south side of the jet and the presence of the shortwave trough on the north side of the jet. East of the upper-level trough, a surface low developed in Arkansas and Missouri and broad 850-hPa winds near 15 m s^{-1} were in place from the Mississippi River

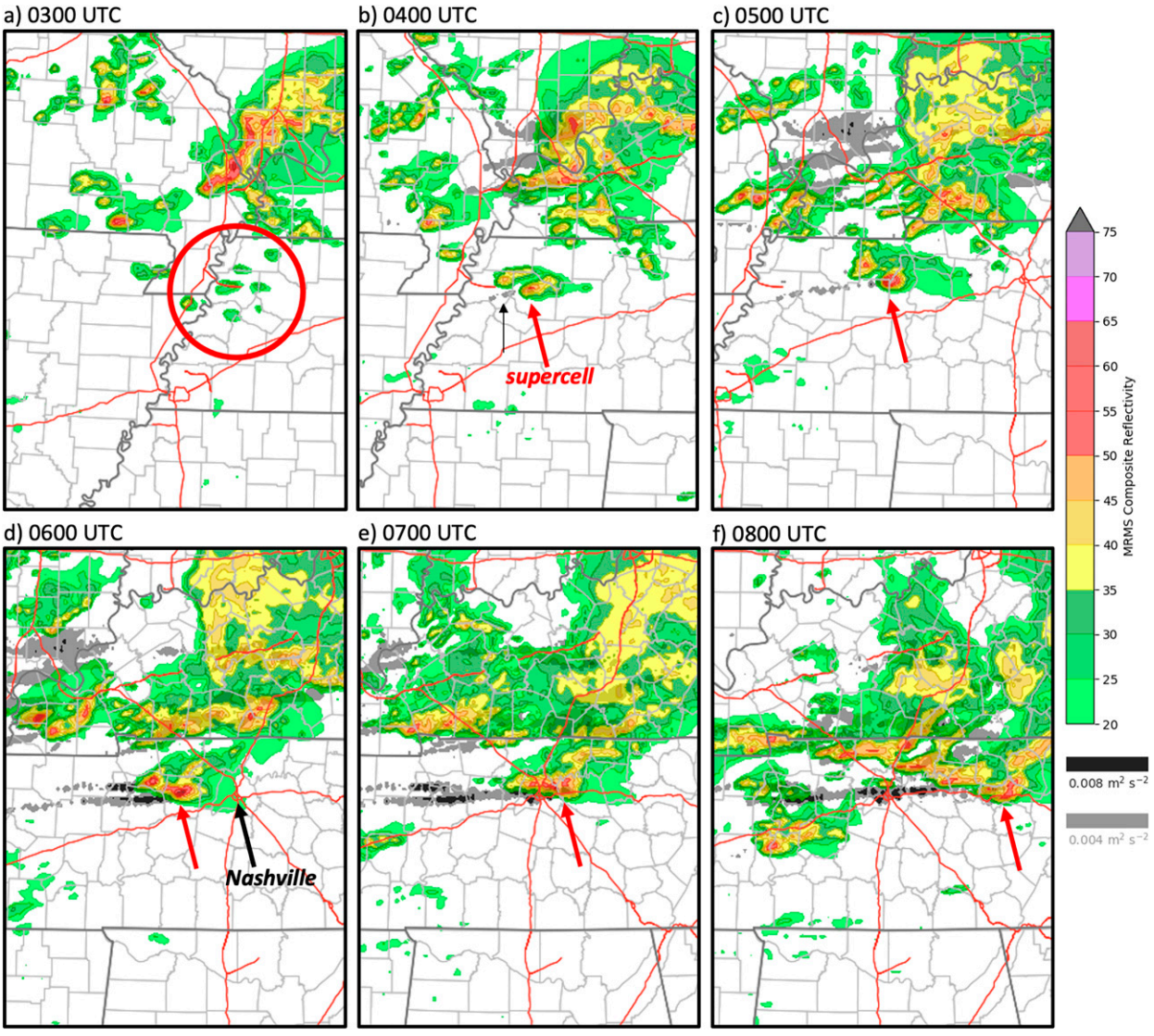

FIG. 3. MRMS composite reflectivity (shaded according to the color bar; dBZ) and accumulated azimuthal wind shear in the 0–2-km layer since 0300 UTC (shaded in gray at 0.004 m^2 s^{-2} and black at 0.008 m^2 s^{-2}) at (a) 0300, (b) 0400, (c) 0500, (d) 0600, (e) 0700, and (f) 0800 UTC 3 Mar 2020. The location of Nashville is marked by the black arrow in (d). The Nashville tornado parent supercell is marked by the red arrow in (b)–(f). The region where the Nashville supercell develops after 0300 UTC is marked by the unfilled red circle in (a). The initial swath of azimuthal shear is marked by the thin black arrow in (b).

east through Tennessee (Fig. 4d). By 0600 UTC 3 March, the center of the upper-level trough was located along the Missouri–Illinois border and a MCS (marked by the region of 500-hPa ascent and 250-hPa divergent outflow) was ongoing in Kentucky east of this trough (Fig. 4e). The 250-hPa jet wind speed increased to over 85 m s^{-1} just south of the upper-level trough. Concurrently, the surface low deepened in the left exit region of the strengthening jet streak as it moved east into western Kentucky and the 850-hPa winds in Tennessee veered to westerly and strengthened to just over 25 m s^{-1} (Fig. 4f). In all, the parent supercell initiated and moved east across Tennessee in a synoptic-scale environment marked by an intensifying 250-hPa jet streak and 850-hPa low-level winds, and weak warm advection in a relatively moist environment over much of Tennessee.

b. *Elevated mixed layer*

Radiosonde observations at 0000 UTC 3 March showed the presence of high lapse rates in the 800–600-hPa layer at Little Rock, Arkansas (LZK; Fig. 5a). The high lapse rates were associated with an elevated mixed layer (EML). Strong westerly flow was present through a deep layer, with veering winds indicative of warm advection below 800 hPa. Farther east at Nashville, Tennessee (BNA), the atmosphere was cooler and

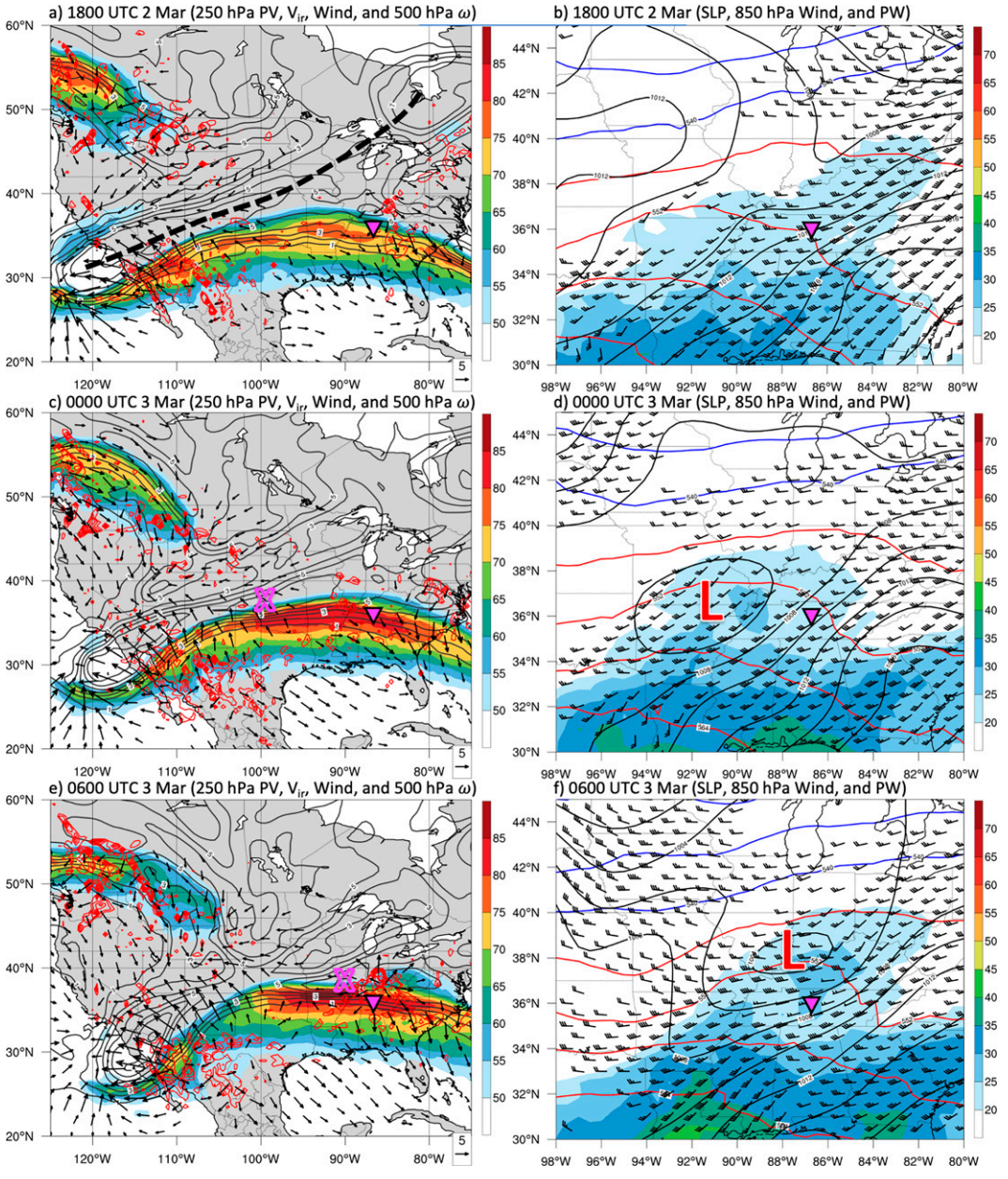

FIG. 4. GFS analysis (left) 250-hPa PV (gray contours every 1×10^{-6} K kg^{-1} m^2 s^{-1}), wind speed (shaded according to the color bar; m s^{-1}), vector divergent wind (arrows $\geq$ 3 m s^{-1}), and 600–400-hPa layer-mean ascent (red contours every 0.5 Pa s^{-1} starting at -0.5 Pa s^{-1}) at (a) 1800 UTC 2 Mar, (c) 0000 UTC 3 Mar, and (e) 0600 UTC 3 Mar 2020. (right) Sea level pressure (black contours every 2 hPa), 850-hPa vector wind (half barb = 2.5 m s^{-1}, full barb = 5 m s^{-1}, pennant = 25 m s^{-1}), 1000–500-hPa thickness (solid contours every 6 dam, blue $\leq$ 540 dam, red $>$ 540 dam), and total column precipitable water (shaded according to the color bar; mm) at (b) 1800 UTC 2 Mar, (d) 0000 UTC 3 Mar, and (f) 0600 UTC 3 Mar 2020. The location of Nashville is marked by the magenta-filled black triangle. The positively tilted 250-hPa trough is marked by the thick dashed black line in (a). The 250-hPa shortwave trough is marked by the unfilled magenta "X" in (c) and (e). The center of the surface low pressure system is marked by a red-filled white "L" in (d) and (f).

moister below 700 hPa with near-surface southerly winds, as a warm front was located just west of Nashville (Fig. 5b). The HRRR analysis showed that the EML in the 800–600-hPa layer at Little Rock expanded east to Nashville by 0300 UTC in conjunction with strong southwesterly flow (Fig. 5c). Backward air parcel trajectories released at Nashville at 0300 UTC 3 March within the EML showed that the high lapse rates originated farther southwest in New Mexico at 0000 UTC

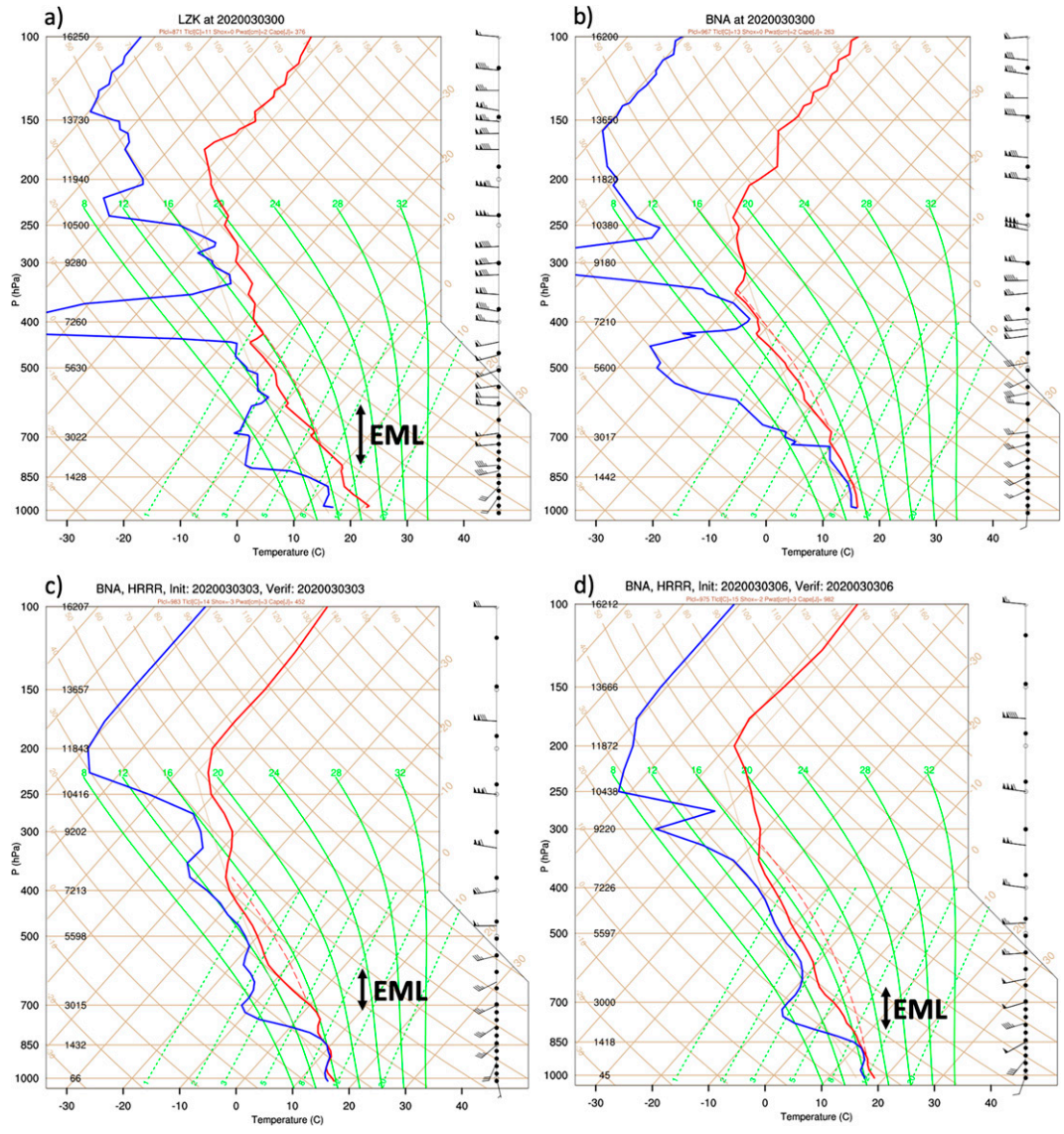

FIG. 5. Skew T–log$p$ diagrams of temperature (red line; °C), dewpoint (blue line; °C), and vector wind (barbs as in Fig. 4b) for observed soundings at 0000 UTC 3 Mar 2020 at (a) LZK and (b) BNA and HRRR analysis soundings at BNA at (c) 0300 and (d) 0600 UTC 3 Mar 2020. The approximate layer of the EML is marked by the black double-sided arrow.

2 March (not shown). Southwesterly flow on the eastern flank of the positively tilted trough in the central United States was key in advecting the EML to Nashville by 3 March. The EML remained in place at 0600 UTC just before the supercell produced an EF3 tornado at Nashville (Fig. 5d). The increase in midlevel lapse rates at Nashville as the EML arrived, combined with warming and moistening of the boundary layer resulted in a marked increase in CAPE during 0000–0600 UTC 3 March (Figs. 5b–d).

For a historical perspective on high lapse rate occurrence at Nashville, all instances were identified in observed 0000 and 1200 UTC soundings at Nashville for 1 January 1979–29 June 2020. High lapse rate soundings were defined as those with a maximum lapse rate ≥ 8.0 K km^{-1} in a 150-hPa-deep layer anywhere between 850 and 400 hPa. High lapse rates occur most frequently at Nashville in February–April, but less than 10% of these soundings are accompanied by an environment considered favorable for thunderstorms[1] (Fig. 6). When considering the February and March 1979–2020 climatology to provide context for the 3 March 2020 EML, 73 out of 853 high lapse rate soundings at Nashville were favorable for

[1] In the climatology, high lapse rate soundings are considered favorable for thunderstorms when both the total totals index $\geq$ 44°C and lifted index $\leq$ 0°C.

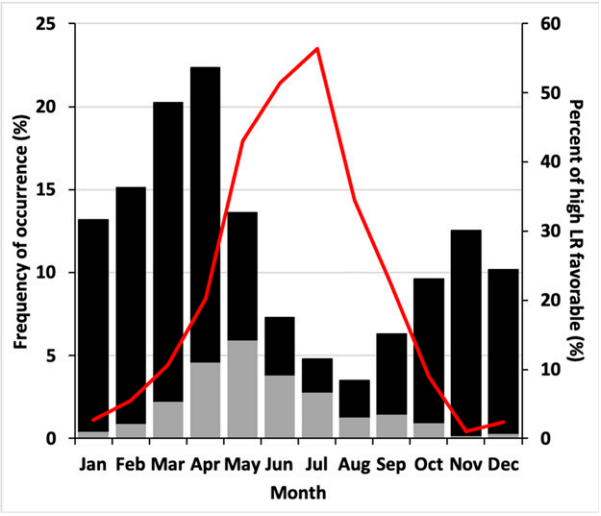

FIG. 6. Frequency of occurrence (%; left axis) of high lapse rates ≥ 8.0 K km^{-1} (black bars) and high lapse rates ≥ 8.0 K km^{-1} with lifted index ≤ 0°C and total totals index ≥ 44°C (gray bars) for all available 0000 and 1200 UTC observed soundings at BNA for 1 Jan 1979–29 Jun 2020. The percentage (%; right axis) of all high lapse rate soundings that have a lifted index ≤ 0°C and total totals index ≥ 44°C is indicated by the red line.

thunderstorms, representing on average <2 soundings per year. The composite-mean 500-hPa height and wind for the 73 high lapse rate events shows anomalous southwesterly flow from the southwest United States and northern Mexico to the Great Lakes region along the forward flank of a positively tilted trough in the central United States and west of anomalously high heights in the eastern United States (not shown). Similar to 2–3 March, this southwesterly flow acts to advect anomalously high lapse rates from the Southwest United States to the Mississippi Valley, and represents a key pathway to observing high lapse rates at Nashville in February and March.

c. *Mesoscale environment*

A manual surface analysis at 0300 UTC 3 March shows mesoscale low pressure centers located in southeast Missouri and southern Illinois near a developing MCS (Fig. 7). From the low center in southeast Missouri, the cold front extends southwest through Arkansas into northeast Texas. A warm front extends southeast into Tennessee and northern Georgia, and separates a region of warm and moist southwest flow in the warm sector and cooler southeast flow over much of Tennessee. A region of showers is located along the warm front in southeast Missouri and western Tennessee, and the supercell will develop within this region of showers by 0330 UTC. A region of 850-hPa frontogenesis located just northeast of the surface warm front suggests that the supercell develops in a region of mesoscale ascent along the warm front (Fig. 8a). On the southwest side of the axis of frontogenesis, 0–1-km vertical wind shear exceeds 20 m s^{-1} and storm-relative helicity (SRH) reaches 350 m^2 s^{-2} and is linked to a 700-hPa cyclonic vorticity maximum (Fig. 8b). In the same region, the deep-layer 0–6-km vertical shear is near 30 m s^{-1} and CAPE exceeds 1250 J kg^{-1} (Fig. 8c). In all, convection initiation occurs in a region where frontogenetical mesoscale ascent overlaps with instability and large vertical wind shear, which favors the rapid development of a supercell.

By 0400 UTC, the supercell was located near the center of the 700-hPa vorticity maximum where instability and vertical shear were maximized near the aforementioned warm front (Figs. 9a,b). The supercell continued eastward toward Nashville through 0600 UTC and remained embedded in a mesoscale environment favorable for supercells that was characterized by enhanced 0–1-km vertical wind shear over 20 m s^{-1}, SRH over 350 m^2 s^{-2}, and CAPE near 1000 J kg^{-1} (Figs. 9c,d). By 0800 UTC, the supercell began to move east of the most favorable thermodynamic environment as CAPE values decreased to less than 500 J kg^{-1}, although the vertical wind shear remained large in conjunction with the 700-hPa vorticity maximum (Figs. 9e,f). The key factor that contributed to the longevity of the supercell with a continued tornado threat was that the favorable thermodynamic and kinematic mesoscale environment moved eastward with the supercell.

From a Eulerian viewpoint, the environment at Nashville evolved rapidly after 0000 UTC 3 March as the supercell approached from the west. The CAPE increased from near 400 J kg^{-1} at 0000 UTC 3 March to near 600 J kg^{-1} by 0500 UTC, and then rapidly increased to near 1000 J kg^{-1} by 0600 UTC when the supercell was located just west of Nashville (Fig. 10a). The increases in CAPE are linked to warming in the lowest 2 km and cooling near 4–5 km AGL, initially (Fig. 10b). Similarly, continued moistening occurred in the lowest 2 km beneath drying in the 2–3-km layer, with drying in response to the arrival of the EML (see also Fig. 5c). The largest increase in CAPE between 0500 and 0600 UTC was driven by warming below 2.5 km (moistening below 2 km) and cooling near 3 km (drying in the 1–3-km layer) as the 700-hPa vorticity maximum approached.

The wind field also evolved rapidly at Nashville after 0000 UTC 3 March. Hourly hodographs for 0300–0700 UTC showed a marked lengthening, particularly in the 0–1-km layer, throughout the period compared to 0000 UTC (Fig. 10c). The evolution of the hodographs is consistent with the larger 0–1-km vertical shear and SRH in the supercell's mesoscale environment that approached from the west (Figs. 9b,d,f). The increases in the 1 km AGL wind speed at Nashville are very similar to the evolution of the geostrophic wind at that level, and suggests that the increase in wind at that level was associated with an increasing pressure gradient with the eastward moving disturbance, rather than a decoupling of the boundary layer from the surface.

In summary, the parent supercell for the Nashville tornado developed in western Tennessee in a mesoscale region of warm frontogenesis where modest CAPE and large vertical wind shear was present near the center of a 700-hPa vorticity maximum. The warm front and 700-hPa vorticity maximum were important contributors to the favorable mesoscale environment that the supercell was embedded in. The supercell remained near the center of the 700-hPa vorticity maximum as it moved eastward across Tennessee through 0700 UTC. A key

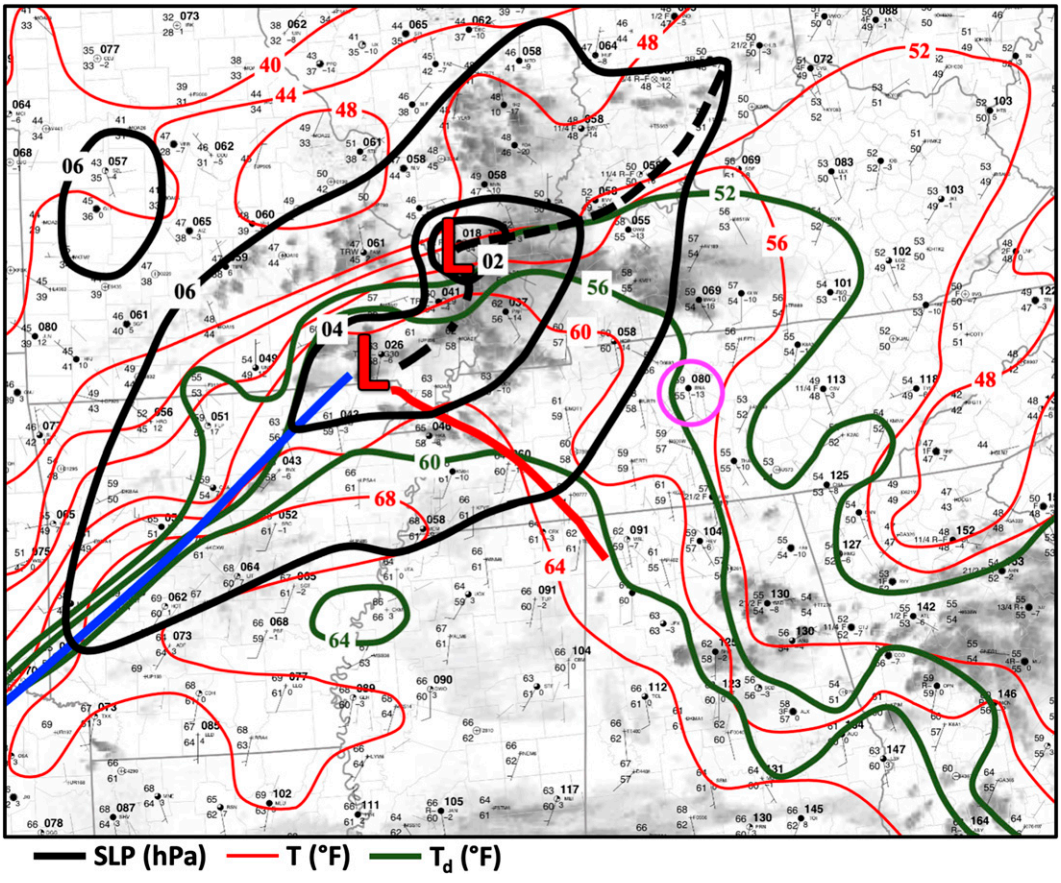

FIG. 7. Manual analysis of sea level pressure (solid black contours every 2 ≤ 1006 hPa), temperature (solid red contours every 4°F), and dewpoint (solid green contours every 4° ≥ 52°F) at 0300 UTC 3 Mar 2020. Surface low pressure centers are marked by a red-filled black "L," troughs of low pressure by a dashed black line, convection line by a dash–dot black line, cold front by a solid blue line, and warm front by a solid red line. BNA is marked by the unfilled magenta circle.

forecast challenge for this event was anticipating how far east into Tennessee the favorable environment ingredients for supercells would extend during the overnight hours. The eastward progression of the 700-hPa vorticity maximum and the warm front allowed for the favorable conditions for supercells to extend eastward across Tennessee through Nashville and farther east.

5. Short-term prediction with WoFS

The aim of this section is to examine the WoFS forecasts for the 2–3 March 2020 nocturnal tornado outbreak and to determine if a retrospective WoFS forecast would have had the potential to add value to the forecast and nowcast process and help extend the lead time of the tornado threat in Nashville. An emphasis will be placed on the period from initiation of the parent supercell at 0330 UTC in western Tennessee through the time of the Nashville tornado at 0630–0700 UTC.

a. Overview of WoFS prediction of Nashville supercell

Two sets of 3-h WoFS forecasts are examined here that are initialized 1) after the supercell initiated and 2) before the supercell initiated. The 3-h forecasts initialized at 0400, 0500, and 0600 UTC 3 March—after the supercell formed—are summarized in Fig. 11. The ensemble probability matched mean (PM; Clark 2017, and references therein) composite reflectivity for all three forecasts verifying at 0700 UTC showed a region of 50-dBZ reflectivity in the Nashville area that extended northeastward into Kentucky. A swath of high probability of updraft helicity (UH; Kain et al. 2008) in the 0–2-km layer ≥ 20 m^2 s^{-2} extended from the location of the supercell at the initial time through Nashville at 0700 UTC. The probability reached as high as 80% in the forecast initialized at 0400 UTC, and increased to over 90% in the forecasts initialized at 0500 and 0600 UTC. The ensemble maximum UH in the 0–2-km layer exceeded 60 m^2 s^{-2} in the Nashville area in each forecast (not shown). In all, the WoFS forecasts initialized at 0400–0600 UTC all indicated a high probability of a supercell storm with strong low-level rotation near Nashville between 0630 and 0700 UTC. Given the typical latency in the WoFS forecast information in real-time mode, the 0400 UTC initialization hypothetically would have been available to forecasters by 0430 UTC and possibly contribute to the

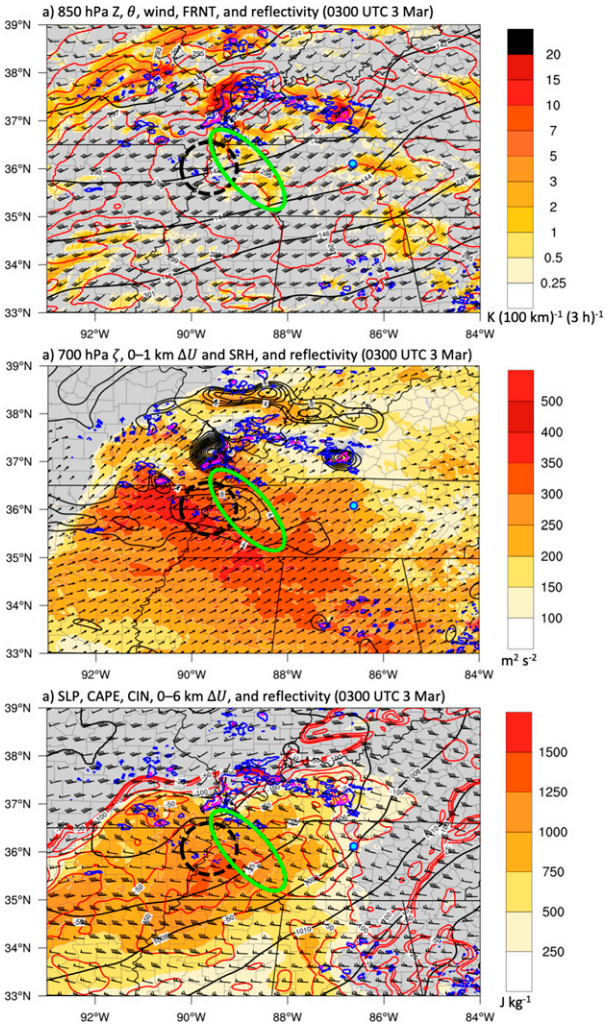

FIG. 8. (a) 850-hPa geopotential height (black contours every 2 dam), potential temperature (red contours every 1 K), wind (barbs as in Fig. 4b), and frontogenesis [shaded according to the color bar; K (100 km)$^{-1}$ (3 h)$^{-1}$], and (b) 700-hPa relative vorticity (black contours every 2×10^{-5} s^{-1} starting at 4×10^{-5} s^{-1}) and 0–1-km vertical wind shear (arrows in ≥10 m s^{-1}), and (c) sea level pressure (black contours every 2 hPa), CIN (red contours every 25 J kg^{-1}), 0–6-km vertical wind shear (barbs as in Fig. 4b), and CAPE (shaded according to the color bar; J kg^{-1}) at 0300 UTC 3 Mar 2020. MRMS base reflectivity (blue contours at 35 dBZ and magenta at 50 dBZ) is overlaid on each panel. The axis of frontogenesis is marked by the unfilled green oval and the convection initiation region by the unfilled black dashed circle. BNA is marked by the light blue filled blue circle.

nowcasting process ~50 min prior to issuance of the tornado watch for the Nashville metropolitan area.

The 3-h forecasts initialized at 0100, 0200 and 0300 UTC 3 March—before the supercell formed—are summarized in Fig. 12. The forecast initialized at 0100 UTC showed a PM object in western Tennessee just east of the Mississippi River at 0400 UTC (Fig. 12a). This PM object was associated with a swath of probabilities of 0–2-km UH ≥ 20 m^2 s^{-2} near 30% that began in northeast Arkansas and extended into western Tennessee. The observed supercell was located farther northeast compared to the ensemble forecasted PM object at 0400 UTC. While the 0100 UTC WoFS forecast indicated potential for a supercell near the correct location of the observed supercell at 0400 UTC, the evolution of the storm in the forecast did not match observations. In the WoFS forecast, the supercell storm initiated in eastern Arkansas and moved east into Tennessee, while the observed storm initiated in western Tennessee. In fact, observed supercells did not occur at all in Arkansas.

For the WoFS forecasts initialized at 0200 and 0300 UTC, probabilities of 0–2-km UH ≥ 20 m^2 s^{-2} were relatively low near 10% in western Tennessee for the forecast period ending at 0500 UTC (Figs. 12b,c). The observed supercell was located west of Nashville and north of Interstate-40 at 0500 UTC (Figs. 3c and 12b,c). The 40-dBZ "paintballs" showed that some of the WoFS individual ensemble members had reflectivity objects near and east of the observed supercell storm (Figs. 12b,c), and the ensemble maximum 0–2-km UH exceeded 60 m^2 s^{-2} near Interstate-40 west of Nashville (not shown). The WoFS forecasts initialized at 0100–0300 UTC had a much lower probability of occurrence for supercells along Interstate-40 west of Nashville through 0500 UTC compared to later initializations (Figs. 11 and 12). However, the ensemble maximum 0–2-km UH for all forecasts initialized at 0100–0600 UTC had similar values that exceeded 60 m^2 s^{-2}. In all, the WoFS forecasts evolved from a low probability, high severity scenario in the 0100–0300 UTC initializations to a high probability, high severity scenario in the 0400–0600 UTC initializations.

b. *WoFS ensemble analysis of Arkansas supercells*

1) OVERVIEW AND METHODS

A key aspect of the WoFS forecasts initialized prior to the development of the Nashville tornado parent supercell was that the predicted supercells originally developed in Arkansas and then moved eastward into Tennessee (Fig. 12). This evolution differed from observations, where the parent supercell developed east of the Mississippi River in western Tennessee, and supercell storms did not occur in Arkansas (Figs. 3a,b). This persistent forecast error in pre-convection initiation WoFS forecasts motivates investigation of the factors that contributed to the development of supercells in Arkansas in the WoFS forecasts. For example, the forecast from WoFS ensemble member 1 initialized at 0300 UTC begins with a supercell in eastern Arkansas that moved eastward in the forecast and produced a 0–2-km UH swath along Interstate-40 approaching Nashville at 0600 UTC (not shown). This ensemble member represented the worst-case scenario of the low probability, high severity ensemble forecast from the 0300 UTC initialization. The supercell in Arkansas in the initial conditions at 0300 UTC was inherited from the 1-h forecast from the 0200 UTC initialization. Likewise, this supercell in the initial conditions at 0200 UTC was inherited from the 1-h forecast from the 0100 UTC initialization, and so on. The origin of this supercell can be traced back to the 0000 UTC

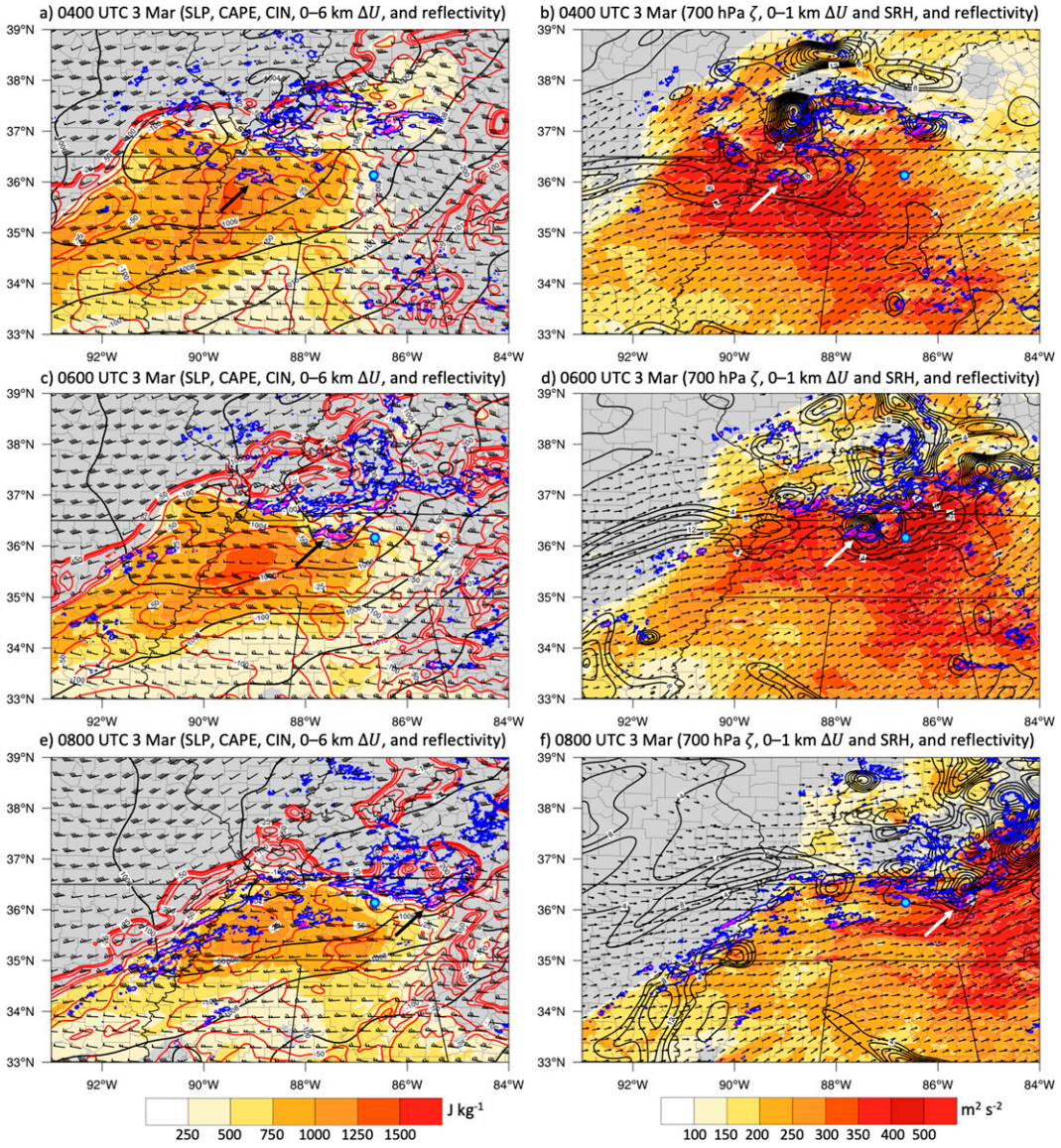

FIG. 9. (left) As in Fig. 8c, except at (a) 0400, (c) 0600, and (e) 0800 UTC 3 Mar 2020. (right) As in Fig. 8b, except at (b) 0400, (d) 0600, and (f) 0800 UTC 3 Mar 2020. The thick arrow points to the supercell.

initialization where it appeared in the 1-h forecast on the western edge of the model domain (recall Fig. 2).

Because not all WoFS members produced supercells in Arkansas, it is of interest to examine in more detail why some members produced these supercells and some did not. Manual inspection of each ensemble member in all of the WoFS forecasts initialized from 2000 UTC 2 March to 0300 UTC 3 March revealed that the supercells in Arkansas first appeared in the 0100–0200 UTC time frame in the 2300 and 0000 UTC initializations either by initiating within the WoFS domain or moving into the WoFS domain through the HRRRE lateral boundary conditions as discussed above with WoFS ensemble member 1. A time-lagged ensemble approach that used all WoFS members from the 2300 and 0000 UTC initializations was used to compare the WoFS members that produced supercells in Arkansas to those members that did not. The area-averaged maximum UH in the 2–5-km layer in the period verifying at 0100–0200 UTC was used as the forecast metric (UH_m) to separate WoFS members with and without supercells in Arkansas. Previous studies have used UH and other metrics in ensemble sensitivity analyses (Kerr et al. 2019; Trier et al. 2021), such as vertical eddy kinetic energy (e.g., Torn et al. 2017; Berman et al. 2017) and precipitation-based metrics (e.g., Torn and Romine 2015), but UH_m is used here because it better discriminates against the presence of supercell storms. Furthermore, UH_m is used instead of object-based supercell tracking (e.g., Britt et al. 2020) since we are interested in the mesoscale environment across

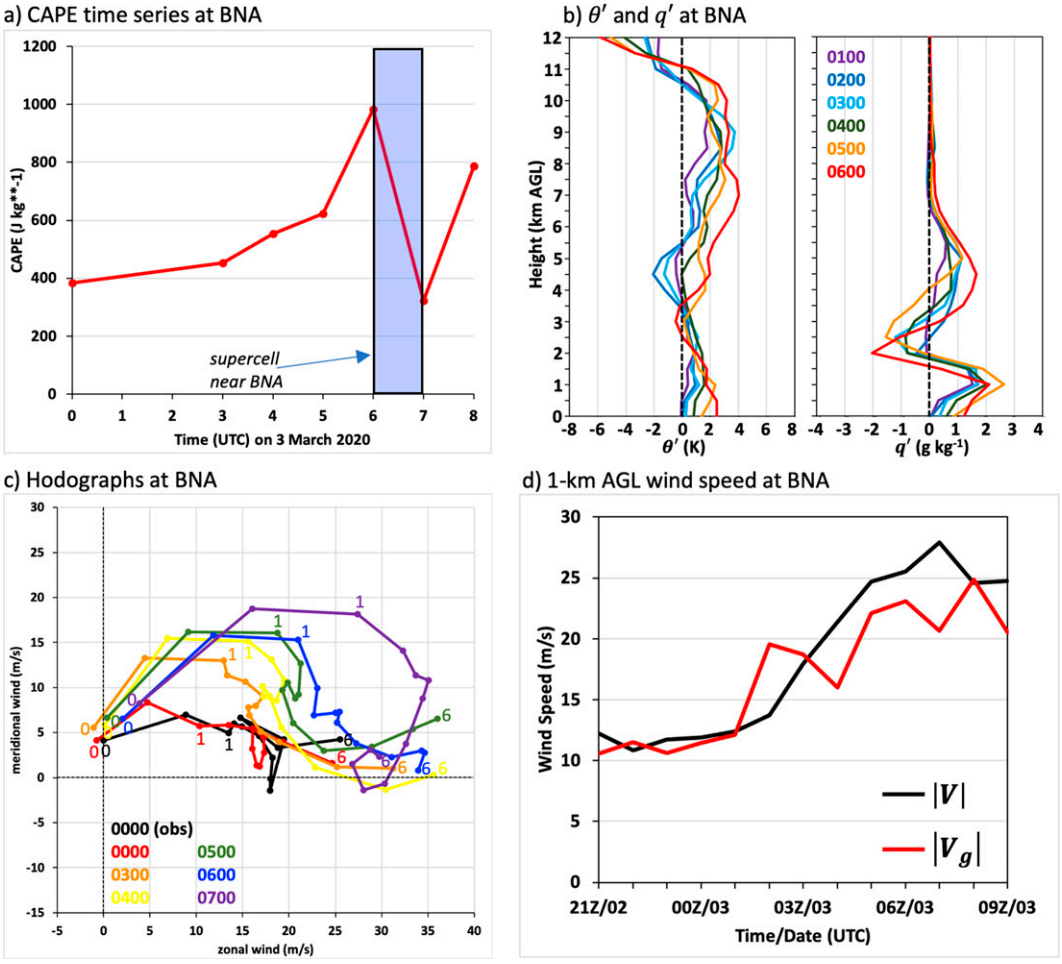

FIG. 10. HRRR analysis-derived (a) time series of CAPE (J kg^{-1}), (b) vertical profiles of potential temperature (θ'; K), and water vapor mixing ratio (q'; g kg^{-1}) perturbations relative to 0000 UTC (lines colored at times according to the key; UTC), (c) hodographs at key times (colored according to the key; UTC), and (d) time series of total wind speed (black; m s^{-1}) and geostrophic wind speed (red; m s^{-1}) at BNA on 3 Mar 2020. In (a), the time in which the parent supercell was near Nashville is marked by the light blue-filled black square. In (c), the hodograph plotted with the black line is derived from observations at BNA as shown in Fig. 5b. All other hodographs are derived from the HRRR analysis.

Arkansas rather than environments in close proximity to specific supercells.

The geographical region used for the area averaging was determined using a similar method introduced by Torn et al. (2017, their section 4) that was based on the standard deviation of UH_m among the ensemble members. For all 36 time-lagged ensemble members, UH_m for the 0100–0200 UTC period was calculated at each grid point, and then spatially smoothed. Then, the standard deviation of the smoothed UH_m among the time-lagged ensemble members was calculated at each grid point. The UH_m area was defined as all of the grid points that have a standard deviation $\geq 50\%$ of the maximum standard deviation grid point value. This area identified regions of greatest variability in UH_m in the ensemble and helped focus on areas where some ensemble members produced supercells and others did not. Figure 13 shows the UH_m metric region overlaid on the WoFS time-lagged ensemble members with the largest and smallest metric values. The metric area calculation identified regions of largest UH_m variability in northeast Arkansas and southeast Missouri. All of the WoFS ensemble members produced supercell storms in Missouri, so the source of variability in the metric calculation in that region is derived from differences in the location of the highest UH values (not shown). In Arkansas, however, the variability was more strongly linked to whether WoFS members produced supercells or not. The portion of the metric area that is located in Arkansas, extreme southeast Missouri, and western Tennessee south of the latitude of the Tennessee–Kentucky border (shown in black) was used in the ensemble sensitivity analysis because it directly addresses the Arkansas supercells. The WoFS ensemble member with the highest metric value has two supercells in northern Arkansas and a second region of convection farther south just west of the

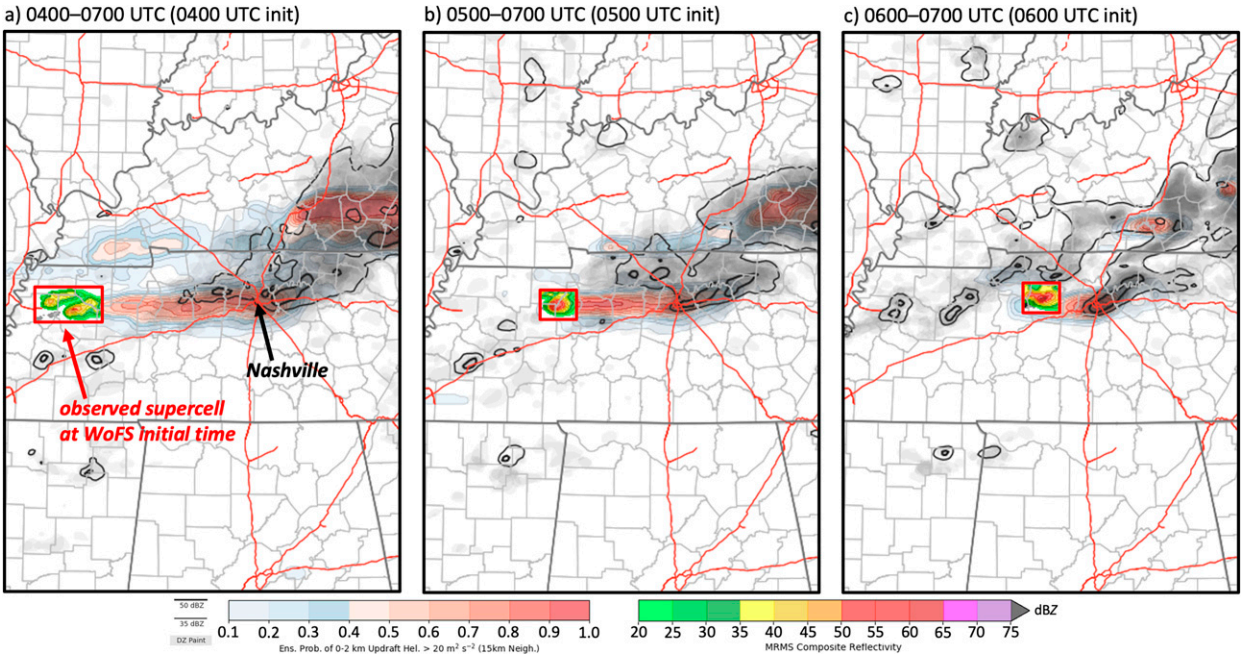

FIG. 11. WoFS ensemble probability of UH in the 0–2-km layer ≥ 20 $m^2 s^{-2}$ (shaded according to the left color bar), reflectivity ≥ 40 dB*Z* paintballs (gray shading), and PM reflectivity (thick contours at 35 and 50 dB*Z*) for (a) 0400–0700 UTC for the forecast initialized at 0400 UTC, (b) 0500–0700 UTC for the forecast initialized at 0500 UTC, and (c) 0600–0700 UTC for the forecast initialized at 0600 UTC 3 Mar 2020. MRMS reflectivity (shaded according to the right color bar; dB*Z*) of the Nashville tornado parent supercell at the WoFS initial time is shown in the inset in each panel.

Mississippi River at 0130 UTC 3 March (Fig. 13a). Conversely, the WoFS ensemble member with the smallest metric value had no convection in Arkansas at 0130 UTC, which was more consistent with observations (Figs. 13b,c).

A summary of the WoFS ensemble member boundary conditions and physics options is provided in Table 3. To assess to what extent the pre-storm environment among the ensemble members governed the presence of supercells in Arkansas,

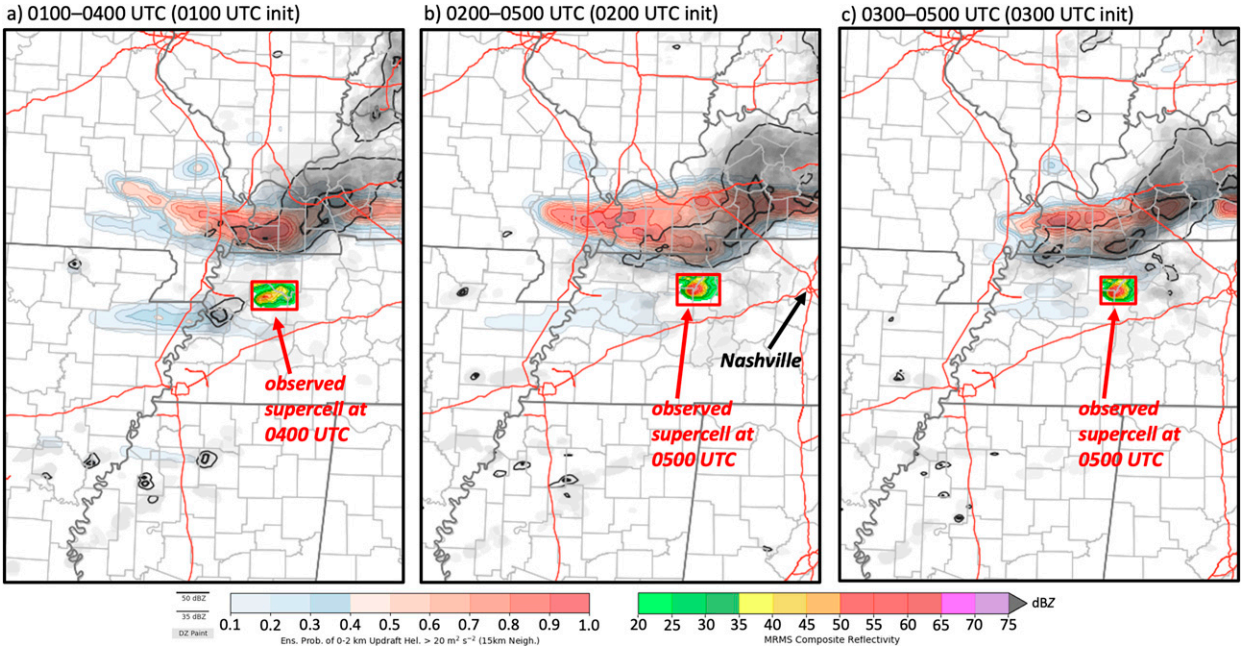

FIG. 12. As in Fig. 11, but for (a) 0100–0400 UTC for the forecast initialized at 0100 UTC, (b) 0200–0500 UTC for the forecast initialized at 0200 UTC, and (c) 0300–0500 UTC for the forecast initialized at 0300 UTC 3 Mar 2020. MRMS reflectivity (shaded according to the right color bar; dB*Z*) of the Nashville tornado parent supercell is shown in the inset at (a) 0400, (b) 0500, and (c) 0500 UTC 3 Mar 2020.

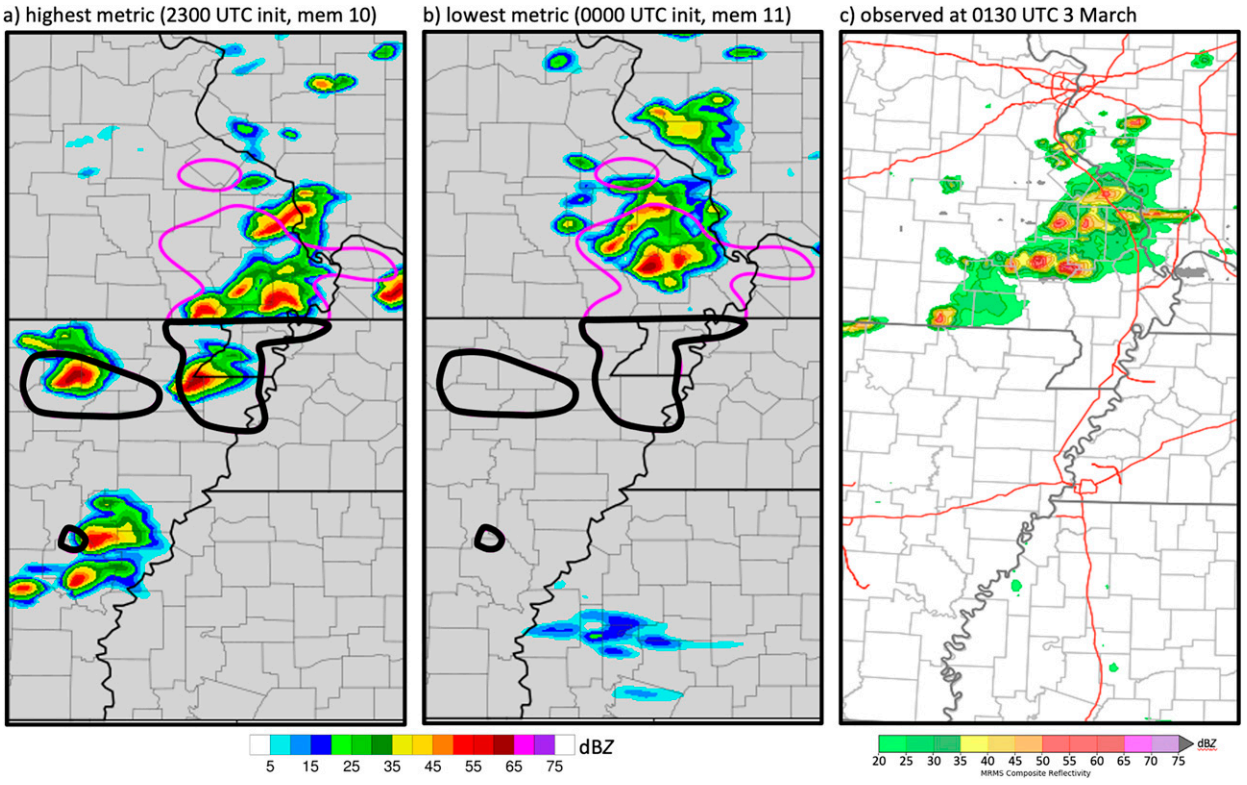

FIG. 13. WoFS 1 km AGL reflectivity (shaded according to the left color bar; dBZ) verifying at 0130 UTC 3 Mar 2020 for ensemble (a) member 10 initialized at 2300 UTC and (b) member 11 initialized at 0000 UTC. (c) MRMS composite reflectivity (shaded according to the right color bar in dBZ) and azimuthal wind shear in the 0–2-km layer (shaded in gray at 0.004 m^2 s^{-2} and black at 0.008 m^2 s^{-2}) at 0130 UTC 3 Mar 2020. The regions bounded by the thick black line mark the portion of the forecast metric region (otherwise shown in magenta) in Arkansas, southeast Missouri, and western Tennessee used in the WoFS ensemble member comparison.

the 10 members with the largest UH_m value were compared to the 10 members with the smallest UH_m value. A bootstrap resampling method described in Torn and Romine (2015) was used to determine the statistically significant differences in the composite means of the two groups. Two groups of 10 members were randomly selected from the full 36-member WoFS time-lagged ensemble and the differences of ensemble mean quantities of the two subsets were calculated, which follows methods used in previous studies (e.g., Galarneau and Hamill 2015). This procedure was repeated 10 000 times to determine the 95% confidence bounds on the composite mean differences.

2) Influence of environment on supercells in WoFS domain

Comparison of the pre-storm environment conditions among members in the UH_m metric region verifying at 0000 UTC, 1–2 h prior to the occurrence of supercells, reveals that members with supercells had environments more favorable for convection with increased water vapor and reduced stability. Figure 14 shows that members with supercells in the UH_m metric region were characterized by significantly higher equivalent potential temperature through a deep layer at 0000 UTC compared to members without supercells. The significantly higher equivalent potential temperature below 800 hPa was associated with either higher potential temperature (in the 900–800-hPa layer) or higher water vapor mixing ratio (near 900 hPa). Higher equivalent potential temperature was associated with higher water vapor mixing ratio values above 800 hPa. In addition to increased water vapor, steeper lapse rates were evident in the 850–700-hPa layer for members that produced supercells in the metric region, with higher potential temperatures near 850 hPa and lower potential temperatures near 700 hPa.

Figure 15 summarizes the spatial distribution of composite mean differences at 0000 UTC 3 March. The WoFS members with supercells in Arkansas had a broad region of higher water vapor mixing ratio at 900 hPa and higher potential temperature at 850 hPa in northeast Arkansas (Figs. 15a,b). The warmer and more moist conditions were located within a region of enhanced low level southerly flow at 900 hPa located on the southern flank of an axis of frontogenesis that extended northern Arkansas to southeast Tennessee (Fig. 15c). The observed supercell formed in a region of frontogenesis in western Tennessee at 0330 UTC, and the ensemble sensitivity analysis suggests that WoFS members that produced supercells earlier in the evening in Arkansas had not only better thermodynamics, but also stronger warm

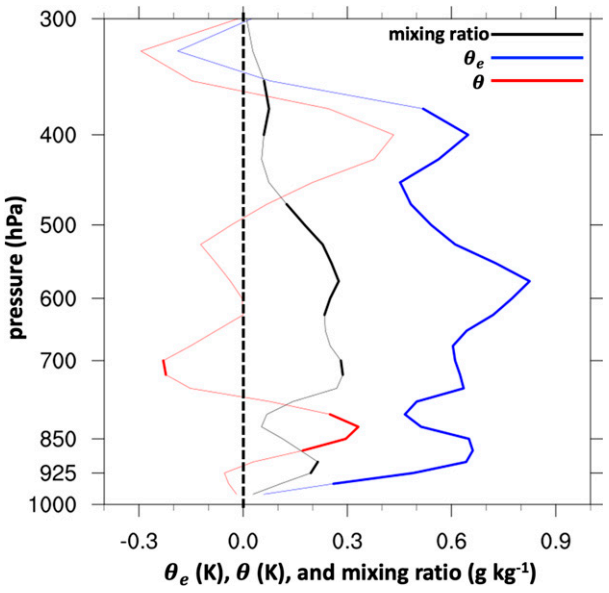

FIG. 14. Vertical profile of the difference in the mean water vapor mixing ratio (black line; g kg^{-1}), potential temperature (red line; K), and equivalent potential temperature (blue line; K) in the forecast metric region shown in Figs. 13a and 13b for the 10 members with the largest UH_m minus the 10 members with the smallest UH_m at 0000 UTC 3 Mar 2020. The thick lines mark the pressure levels in which the difference is statistically significant at the 95% level using bootstrap resampling without replacement. The dashed black line marks zero.

frontogenesis and inferred mesoscale ascent. It was likely that these more favorable conditions in Arkansas were linked, in part, to a slower moving surface low positioned farther southwest in the HRRRE boundary conditions.

3) INFLUENCE OF LATERAL BOUNDARY CONDITIONS ON SUPERCELLS IN WOFS DOMAIN

The WoFS ensemble member forecast metric stratified by model physics and boundary conditions is shown in Fig. 16. Each combination of model PBL and radiation physics was used for 6 ensemble members as summarized in Table 3. A wide variety of forecast solutions in the metric region occurred for each combination of model physics schemes, except for the MYNN/Dudhia PBL and radiation physics combination that systematically resulted in a lower metric value (Fig. 16). The WoFS forecasts that used HRRRE members 1, 4, and 9 as boundary conditions produced the highest forecast metric on average (Fig. 16). The WoFS forecasts that used HRRRE members 2, 3, and 5 produced the lowest forecast metric overall. The actual HRRRE forecasts from members 1, 4, and 9 produced supercells in Arkansas, while members 2, 3, and 5 did not. Example forecasts of reflectivity and 0–2 km UH from HRRRE members 1 and 2 verifying at 0200 UTC 3 March are shown in Figs. 17a and 17b. Comparison of the thermodynamic environment showed significantly higher CAPE throughout much of eastern Arkansas in HRRRE members 1, 4, and 9 versus members 2, 3, and 5 (Fig. 17c). These results suggest that while WoFS model PBL and radiation physics combinations may have had a secondary influence on the development of supercells in Arkansas, the HRRRE boundary conditions played a larger role by influencing the thermodynamic environment in Arkansas and directly moving supercells from the HRRRE forecast into the WoFS domain.

To further test the influence of the boundary conditions on the movement of supercells into the WoFS domain, the WoFS forecast with the largest metric (member 10 initialized at 2300 UTC) and smallest metric (member 11 initialized at 0000 UTC) were rerun with alternative boundary conditions (Table 3). WoFS member 10 used HRRRE member 1 for boundary conditions and produced a metric value of 10.9 m^2 s^{-2}, and when rerun using HRRRE member 2 as boundary conditions, the metric decreased to 6.5 m^2 s^{-2}. WoFS member 11 used HRRRE member 2 and produced a metric of 0.0 m^2 s^{-2}. When WoFS member 11 was rerun using HRRRE member 1, however, the metric increased to 1.9 m^2 s^{-2}. In all, these additional simulations highlight the influence of the HRRRE boundary conditions in moving supercells into the WoFS domain.

6. Summary and conclusions

This study presents a multiscale analysis of the nocturnal significant tornado outbreak in Tennessee on 2–3 March 2020. This tornado outbreak occurred in conjunction with a long-lived supercell that initiated in western Tennessee at 0330 UTC 3 March and moved east along and just north of Interstate-40 through 0900 UTC. The supercell produced numerous tornadoes, including six significant tornadoes, three of which resulted in fatalities. Included in this outbreak was an EF3 tornado that struck the northern part of the Nashville, Tennessee, metropolitan area resulting in 5 fatalities and 220 injuries and an EF4 tornado that moved through Cookeville, Tennessee, resulting in 19 fatalities and 87 injuries. In addition to documenting the life cycle of the parent supercell and its surrounding environment, this study conducted a time-lagged ensemble sensitivity analysis to explore the short-term prediction of the parent supercell from the NSSL WoFS convection-allowing ensemble. This investigation of WoFS is motivated by the forecast challenges that are brought with significant tornadoes that occur at night when the public is more vulnerable and less likely to receive information on watches and warnings during the overnight hours (Ashley et al. 2008; Ellis et al. 2020).

There were several aspects of the synoptic and mesoscale flow that favored the development of a long-lived supercell in Tennessee. First, the synoptic-scale trough over the United States was positively tilted, which allowed for southwesterly flow to advect high lapse rates in the form of an EML from the southwest United States to the Mississippi Valley. High lapse rates with environments that favor thunderstorms are relatively rare at Nashville in February and March. In this case, a warm front brought a warm, moist boundary layer to Nashville and when combined with cold temperatures aloft

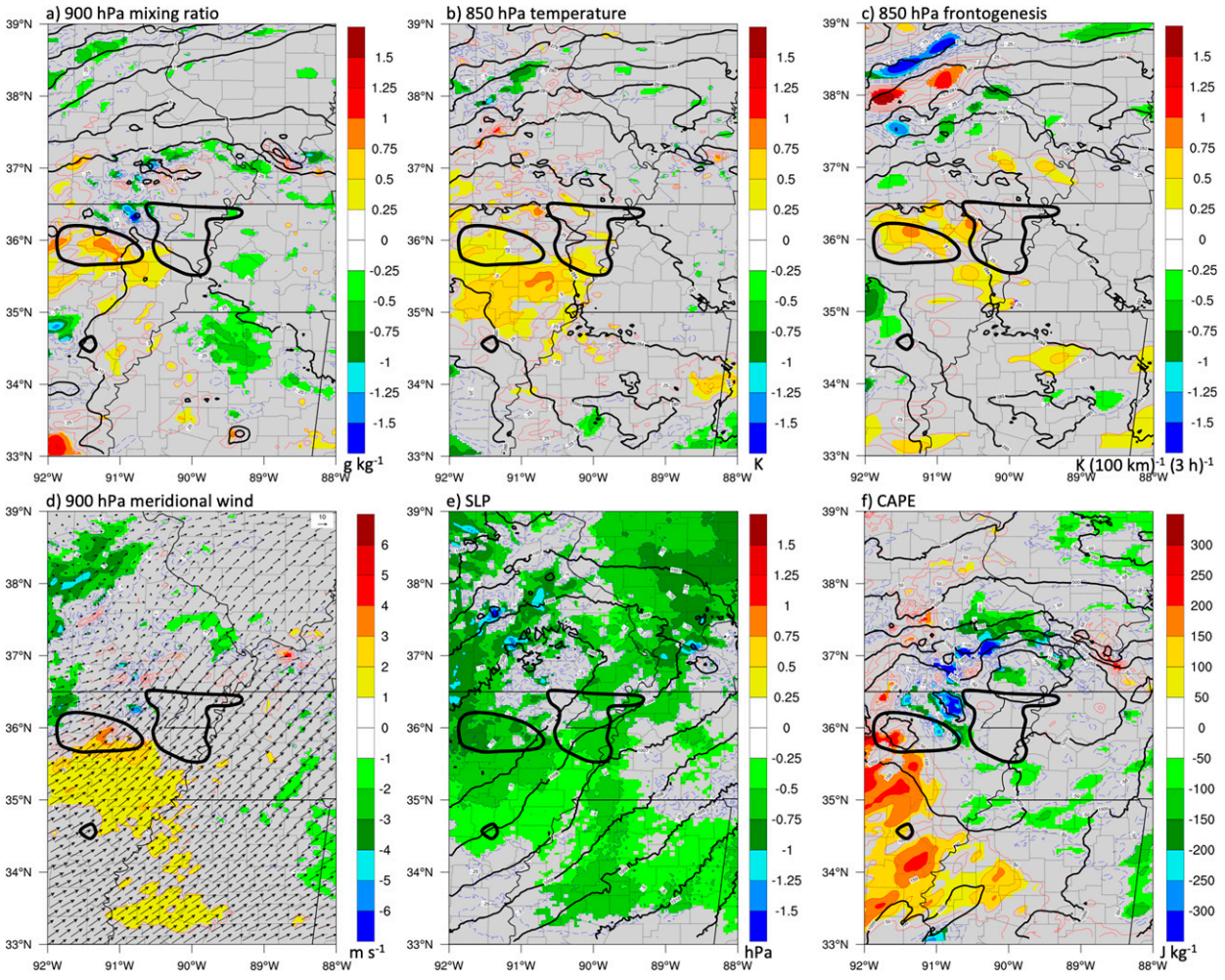

FIG. 15. Differences (10 members with the largest UH_m minus the 10 members with the smallest UH_m) in (a) 900-hPa water vapor mixing ratio (g kg^{-1}), (b) 850-hPa temperature (K), (c) 850-hPa frontogenesis [K (100 km)$^{-1}$ (3 h)$^{-1}$], (d) 900-hPa meridional wind (m s^{-1}), (e) sea level pressure (hPa), and (f) CAPE (J kg^{-1}) between the two ensemble groups at 0000 UTC. Each panel shows the full 36-member ensemble mean in black contours and the difference in thin contours (blue dashed negative, solid red positive) shaded according to the color bar where significant at the 95% level using bootstrap resampling without replacement. In (d), the ensemble mean vector wind is shown. The regions bounded by the thick black lines mark the forecast metric region used in the WoFS ensemble member comparison.

(500-hPa temperature near −20°C) above the EML, resulted in CAPE values higher than what is typically observed for HSLC events. Second, a 250-hPa jet streak strengthened in conjunction with an increasing PV gradient due to the eastward movement of a mesoscale PV maximum on the north side of the jet and negative advection of PV by the divergent wind on the south side of the jet. The northward divergent wind was driven, in part, by widespread convection over northern Mexico and south Texas. A midlevel disturbance and attendant deepening surface low in the left exit region of the intensifying 250-hPa jet streak resulted in a marked acceleration of the westerly low-level flow in Tennessee after 0000 UTC 3 March. As a result, the low-level vertical wind shear and SRH increased similar to previous nocturnal significant tornado events (e.g., Kis and Straka 2010), favoring the development and maintenance of the parent supercell. Previous studies have shown that convective outflow can interact with the upper-level jet by negative PV advection by the divergent wind and lead to jet intensification and trigger Rossby wave trains (e.g., Archambault et al. 2013). Future research will examine how the remote influence of convection on upper-level jet streaks impacts the predictability of the downstream mesoscale environment in this and other cases on 6–24-h time scales.

Earlier WoFS forecasts initialized in the evening between 2100 and 0300 UTC had increased uncertainty in the timing and location of supercell initiation. To better understand why some of the WoFS ensemble members produced erroneous supercells in Arkansas, an ensemble-based sensitivity analysis was performed using a time-lagged ensemble approach for

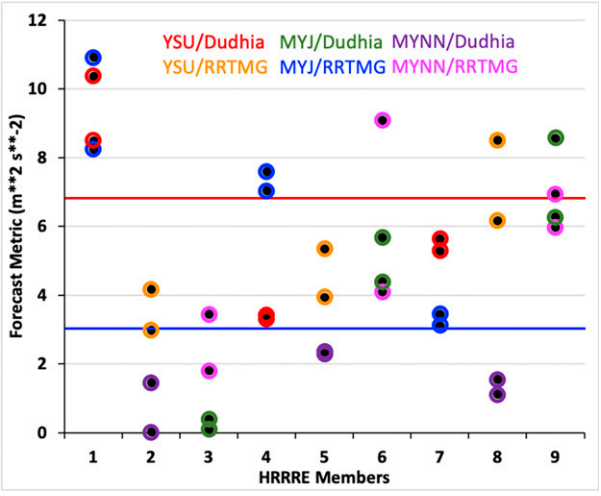

FIG. 16. Area mean forecast metric (m^2 s^{-2}) for all WoFS members initialized at 2300 UTC 2 Mar and 0000 UTC 3 Mar 2020 stratified by HRRRE member boundary condition and colored by the physics options. The red line marks the threshold for the top 10 WoFS ensemble members in terms of forecast metric. The blue line marks the bottom 10 members.

the forecasts initialized at 2300 UTC 2 March and 0000 UTC 3 March. The analysis revealed that the presence of supercells in Arkansas in WoFS was governed by 1) movement of supercells into the WoFS domain and 2) the upstream environment conditions, both of which were driven by the HRRRE boundary conditions. For the environment, ensemble members with supercells in Arkansas were characterized by increased water vapor and instability in and above the boundary layer near the western edge of the WoFS model domain and increased southerly flow at low levels throughout northeast Arkansas. The presence of drier air in the midtroposphere has been shown in previous idealized and real-data numerical modeling studies to limit convective updrafts (James and Markowski 2010; Torn et al. 2017), and the results from the WoFS ensemble appear to be somewhat consistent with those findings. Additionally, WoFS members with supercells had stronger 850-hPa frontogenesis and inferred mesoscale ascent in northern Arkansas. Warm frontogenesis and attendant mesoscale ascent were important in initiating the observed supercell in Tennessee. It appears that the WoFS solution in Arkansas was sensitive to this as well. ASOS and radiosonde observations assimilated into WoFS are not dense enough spatially and frequent enough to correct these errors in the initial conditions. These results suggest that for short-term convection-allowing model forecasts like WoFS that use a relatively small domain there is a need for improved lateral boundary conditions and more thermodynamic observations above the surface particularly near the upstream lateral boundary.

The WoFS ensemble has been run in experimental real-time mode for several years at NSSL and it has shown capability for providing accurate predictions of thunderstorm and landfalling tropical cyclone hazards (e.g., Wheatley et al. 2015; Jones et al. 2016; Skinner et al. 2018; Jones et al. 2019; Flora et al. 2019; Yussouf et al. 2020). Analysis of the nocturnal significant tornado outbreak in Tennessee demonstrates the capability of WoFS to provide useful guidance for nocturnal events in which it is uncertain how far into the overnight hours the tornado threat will persist. While it is difficult to say how the issuance of tornado watches and warnings would have changed for this event if the WoFS guidance was available in real-time, it is clear that WoFS indicated a high probability, high severity tornado threat for the Nashville area ~70 min prior to the tornado watch and ~2 h prior to the first tornado warning that included the Nashville metropolitan area. At issue is whether the lower certainty in earlier WoFS guidance would have delayed recognition of the high probability, high severity solution. The usefulness of WoFS guidance can be stratified into two regimes, pre-convection

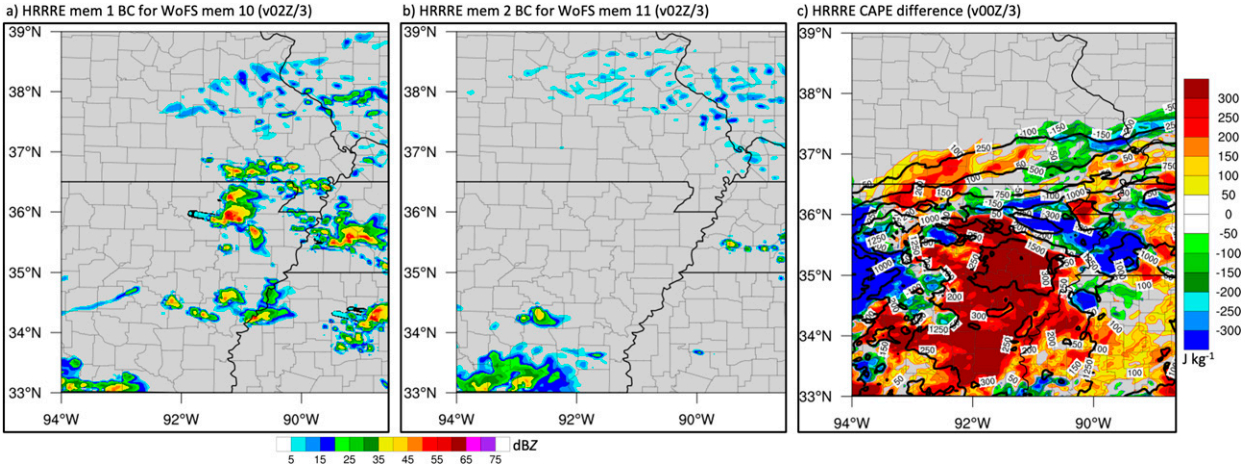

FIG. 17. 1 km AGL reflectivity (shaded according to the left color bar; dBZ) verifying at 0200 UTC 3 Mar 2020 for HRRRE members (a) 1 and (b) 2 initialized at 1200 UTC 2 Mar 2020. (c) Differences (HRRRE members 1, 4, and 9 minus HRRRE members 2, 3, and 5) in CAPE (shaded with contours according to the right color bar; J kg^{-1}) between the two groups verifying at 0000 UTC 3 Mar 2020 overlaid with the 9-member HRRRE mean CAPE (solid contours; J kg^{-1}).

initiation (pre-CI) and postconvection initiation (post-CI). While pre-CI WoFS forecasts had erroneous supercells in Arkansas and indicated a less certain low probability for tornadoes for Nashville, an abrupt shift to a high probability scenario occurred in the post-CI guidance. The unique design of WoFS, which includes assimilation of novel information from radar and satellite data (e.g., Yussouf et al. 2015; Jones et al. 2020), allows for post-CI correction of errors in initial and boundary conditions that plague the pre-CI forecasts. Hence, in application of WoFS to a real-time forecasting and nowcasting scenario, it should be expected that forecasts will improve post-CI.

Acknowledgments. Support was provided by NOAA VORTEX-Southeast and NOAA/OAR under NOAA–University of Oklahoma Cooperative Agreement NA16OAR4320115, U.S. Department of Commerce. Patrick Burke provided comments and perspectives that helped to improve the manuscript. This study benefited from conversations with Erik Rasmussen, Corey Potvin, Krissy Hurley, Chad Gravelle, Dan Hawblitzel, and Brian Carcione. We thank Stephen Corfidi and two anonymous reviewers for their valuable criticisms of the initial manuscript. We also thank Stephen Corfidi for providing manual analyses and interpretations that motivated the generation of our own manual surface analysis in Fig. 7.

Data availability statement. All datasets used in this study are free and publicly available. Storm report, ASOS, and GFS analysis data are available at NOAA NCEI. The following data are available on the NSSL server: HRRR (https://data.nssl.noaa.gov/thredds/catalog/FRDD/HRRR.html), HRRRE (https://data.nssl.noaa.gov/thredds/catalog/FRDD/HRRRE.html), and WoFS (https://data.nssl.noaa.gov/thredds/catalog/FRDD/WoFS.html). Imagery from WoFS forecasts is available at the NSSL WoFS Realtime Viewer (https://wof.nssl.noaa.gov/realtime/). MRMS and radiosonde data were obtained from the Iowa State University Environmental Mesonet archive (https://mesonet.agron.iastate.edu/archive/). WoFS forecasts were generated using the WRF-ARW model (http://wrf-model.org). Calculations were performed using NCL version 6.6.2 (https://www.ncl.ucar.edu).

REFERENCES

Amante, C., and B. W. Eakins, 2009: ETOPO1 1 arc-minute global relief model: Procedures, data sources, and analysis. NOAA Tech. Memo. NESDIS NGDC-24, 25 pp., https://www.ngdc.noaa.gov/mgg/global/relief/ETOPO1/docs/ETOPO1.pdf.

Archambault, H. M., L. F. Bosart, D. Keyser, and J. M. Cordeira, 2013: A climatological analysis of the extratropical flow response to recurving western North Pacific tropical cyclones. *Mon. Wea. Rev.*, **141**, 2325–2346, https://doi.org/10.1175/MWR-D-12-00257.1.

Ashley, W. S., A. J. Krmenec, and R. Schwantes, 2008: Vulnerability due to nocturnal tornadoes. *Wea. Forecasting*, **23**, 795–807, https://doi.org/10.1175/2008WAF2222132.1.

——, A. M. Haberlie, and J. Strohm, 2019: A climatology of quasi-linear convective systems and their hazards in the United States. *Wea. Forecasting*, **34**, 1605–1631, https://doi.org/10.1175/WAF-D-19-0014.1.

Berman, J. D., R. D. Torn, G. S. Romine, and M. L. Weisman, 2017: Sensitivity of northern Great Plains convection forecasts to upstream and downstream forecast errors. *Mon. Wea. Rev.*, **145**, 2141–2163, https://doi.org/10.1175/MWR-D-16-0353.1.

Britt, K. C., P. S. Skinner, P. L. Heinselman, and K. H. Knopfmeier, 2020: Effects of horizontal grid spacing and inflow environment on forecasts of cyclic mesocyclogenesis in NSSL's Warn-on-Forecast System (WoFS). *Wea. Forecasting*, **35**, 2423–2444, https://doi.org/10.1175/WAF-D-20-0094.1.

Bunker, R. C., A. E. Cohen, J. A. Hart, A. E. Gerard, K. E. Klockow-McClain, and D. P. Nowicki, 2019: Examination of the predictability of nocturnal tornado events in the southeastern United States. *Wea. Forecasting*, **34**, 467–479, https://doi.org/10.1175/WAF-D-18-0162.1.

Childs, S. J., R. S. Schumacher, and J. T. Allen, 2018: Cold-season tornadoes: Climatological and meteorological insights. *Wea. Forecasting*, **33**, 671–691, https://doi.org/10.1175/WAF-D-17-0120.1.

Clark, A. J., 2017: Generation of ensemble mean precipitation forecasts from convection-allowing ensembles. *Wea. Forecasting*, **32**, 1569–1583, https://doi.org/10.1175/WAF-D-16-0199.1.

Coffer, B. E., M. D. Parker, R. L. Thompson, B. T. Smith, and R. E. Jewell, 2019: Using near-ground storm relative helicity in supercell tornado forecasting. *Wea. Forecasting*, **34**, 1417–1435, https://doi.org/10.1175/WAF-D-19-0115.1.

Dowell, D. C., and Coauthors, 2016: Development of a High-Resolution Rapid Refresh Ensemble (HRRRE) for severe weather forecasting. *28th Conf. on Severe Local Storms*, Portland, OR, Amer. Meteor. Soc., 8B.2, https://ams.confex.com/ams/28SLS/webprogram/Paper301555.html.

Dudhia, J., 1989: Numerical study of convection observed during the Winter Monsoon Experiment using a mesoscale two-dimensional model. *J. Atmos. Sci.*, **46**, 3077–3107, https://doi.org/10.1175/1520-0469(1989)046<3077:NSOCOD>2.0.CO;2.

Ellis, K., L. R. Mason, and K. Hurley, 2020: In the dark: Public perceptions of and National Weather Service forecaster considerations for nocturnal tornadoes in Tennessee. *Bull. Amer. Meteor. Soc.*, **101**, E1677–E1684, https://doi.org/10.1175/BAMS-D-19-0245.1.

Flora, M. L., P. S. Skinner, C. K. Potvin, A. E. Reinhart, T. A. Jones, N. Yussouf, and K. H. Knopfmeier, 2019: Object-based verification of short-term, storm-scale probabilistic mesocyclone guidance from an experimental Warn-on-Forecast System. *Wea. Forecasting*, **34**, 1721–1739, https://doi.org/10.1175/WAF-D-19-0094.1.

Fuhrmann, C. M., C. E. Konrad II, M. M. Kovach, J. T. McLeod, W. G. Schmitz, and P. G. Dixon, 2014: Ranking of tornado outbreaks across the United States and their climatological characteristics. *Wea. Forecasting*, **29**, 684–701, https://doi.org/10.1175/WAF-D-13-00128.1.

Fujita, T. T., 1981: Tornadoes and downbursts in the context of generalized planetary scales. *J. Atmos. Sci.*, **38**, 1511–1534, https://doi.org/10.1175/1520-0469(1981)038<1511:TADITC>2.0.CO;2.

Galarneau, T. J., Jr., and T. M. Hamill, 2015: Diagnosis of track forecast errors for Tropical Cyclone Rita (2005) using GEFS

reforecasts. *Wea. Forecasting*, **30**, 1334–1354, https://doi.org/10.1175/WAF-D-15-0036.1.

Hong, S.-Y., Y. Noh, and J. Dudhia, 2006: A new vertical diffusion package with an explicit treatment of entrainment processes. *Mon. Wea. Rev.*, **134**, 2318–2341, https://doi.org/10.1175/MWR3199.1.

James, R. P., and P. M. Markowski, 2010: A numerical investigation of the effects of dry air aloft on deep convection. *Mon. Wea. Rev.*, **138**, 140–161, https://doi.org/10.1175/2009MWR3018.1.

Janjić, Z. I., 2002: Nonsingular implementation of the Mellor–Yamada level 2.5 scheme in the NCEP Meso model. NCEP Office Note 437, 61 pp., http://www.emc.ncep.noaa.gov/officenotes/newernotes/on437.pdf.

Jones, T. A., K. Knopfmeier, D. Wheatley, G. Creager, P. Minnis, and R. Palikonda, 2016: Storm-scale data assimilation and ensemble forecasting with the NSSL experimental Warn-on-Forecast System. Part II: Combined radar and satellite data experiments. *Wea. Forecasting*, **31**, 297–327, https://doi.org/10.1175/WAF-D-15-0107.1.

——, P. Skinner, N. Yussouf, K. Knopfmeier, A. Reinhart, and D. Dowell, 2019: Forecasting high-impact weather in landfalling tropical cyclones using a Warn-on-Forecast System. *Bull. Amer. Meteor. Soc.*, **100**, 1405–1417, https://doi.org/10.1175/BAMS-D-18-0203.1.

——, and Coauthors, 2020: Assimilation of *GOES-16* radiances and retrievals into the Warn-on-Forecast System. *Mon. Wea. Rev.*, **148**, 1829–1859, https://doi.org/10.1175/MWR-D-19-0379.1.

Kain, J. S., and Coauthors, 2008: Some practical considerations regarding horizontal resolution in the first generation of operational convection-allowing NWP. *Wea. Forecasting*, **23**, 931–952, https://doi.org/10.1175/WAF2007106.1.

Kerr, C. A., D. J. Stensrud, and X. Wang, 2019: Diagnosing convective dependencies on near-storm environments using ensemble sensitivity analyses. *Mon. Wea. Rev.*, **147**, 495–517, https://doi.org/10.1175/MWR-D-18-0140.1.

Kis, A. K., and J. M. Straka, 2010: Nocturnal tornado climatology. *Wea. Forecasting*, **25**, 545–561, https://doi.org/10.1175/2009WAF2222294.1.

Lakshmanan, V., T. Smith, G. Stumpf, and K. Hondl, 2007: The Warning Decision Support System–Integrated Information. *Wea. Forecasting*, **22**, 596–612, https://doi.org/10.1175/WAF1009.1.

Mansell, E. R., C. L. Ziegler, and E. C. Bruning, 2010: Simulated electrification of a small thunderstorm with two-moment bulk microphysics. *J. Atmos. Sci.*, **67**, 171–194, https://doi.org/10.1175/2009JAS2965.1.

Mellor, G. L., and T. Yamada, 1982: Development of a turbulence closure model for geophysical fluid problems. *Rev. Geophys.*, **20**, 851–875, https://doi.org/10.1029/RG020i004p00851.

Miller, J. E., 1948: On the concept of frontogenesis. *J. Meteor.*, **5**, 169–171, https://doi.org/10.1175/1520-0469(1948)005<0169:OTCOF>2.0.CO;2.

Molina, M. J., J. T. Allen, and V. A. Gensini, 2018: The Gulf of Mexico and ENSO influence on subseasonal and seasonal CONUS winter tornado variability. *J. Appl. Meteor. Climatol.*, **57**, 2439–2463, https://doi.org/10.1175/JAMC-D-18-0046.1.

Nakanishi, M., and H. Niino, 2004: An improved Mellor–Yamada level-3 model with condensation physics: Its design and verification. *Bound.-Layer Meteor.*, **112**, 1–31, https://doi.org/10.1023/B:BOUN.0000020164.04146.98.

——, and ——, 2006: An improved Mellor–Yamada level-3 model: Its numerical stability and application to a regional prediction of advection fog. *Bound.-Layer Meteor.*, **119**, 397–407, https://doi.org/10.1007/s10546-005-9030-8.

NOAA, 2021: NOAA/NCEI storm events database version 3.1. NOAA, accessed 1 February 2021, https://www.ncdc.noaa.gov/stormevents/.

Sherburn, K. D., and M. D. Parker, 2014: Climatology and ingredients of significant severe convection in high-shear, low-CAPE environments. *Wea. Forecasting*, **29**, 854–877, https://doi.org/10.1175/WAF-D-13-00041.1.

——, and ——, 2019: The development of severe vortices within simulated high-shear, low-CAPE convection. *Mon. Wea. Rev.*, **147**, 2189–2216, https://doi.org/10.1175/MWR-D-18-0246.1.

——, ——, J. R. King, and G. M. Lackmann, 2016: Composite environments of severe and nonsevere high-shear, low-CAPE convective events. *Wea. Forecasting*, **31**, 1899–1927, https://doi.org/10.1175/WAF-D-16-0086.1.

Skamarock, W. C., and Coauthors, 2008: A description of the Advanced Research WRF version 3. NCAR Tech. Note NCAR/TN-475+STR, 113 pp., https://doi.org/10.5065/D68S4MVH.

Skinner, P. S., and Coauthors, 2018: Object-based verification of a prototype Warn-on-Forecast System. *Wea. Forecasting*, **33**, 1225–1250, https://doi.org/10.1175/WAF-D-18-0020.1.

Smirnova, T. G., J. M. Brown, S. G. Benjamin, and J. S. Kenyon, 2016: Modifications to the Rapid Update Cycle Land Surface Model (RUC LSM) available in the Weather Research and Forecasting (WRF) Model. *Mon. Wea. Rev.*, **144**, 1851–1865, https://doi.org/10.1175/MWR-D-15-0198.1.

Smith, B. T., J. L. Guyer, and A. R. Dean, 2008: The climatology, convective mode, and mesoscale environment of cool season severe thunderstorms in the Ohio and Tennessee Valleys, 1995–2006. *24th Conf. on Severe Local Storms*, Savannah, GA, Amer. Meteor. Soc., 13B.7, https://ams.confex.com/ams/pdfpapers/141968.pdf.

Smith, T. M., and Coauthors, 2016: Multi-Radar Multi-Sensor (MRMS) severe weather and aviation products: Initial operating capabilities. *Bull. Amer. Meteor. Soc.*, **97**, 1617–1630, https://doi.org/10.1175/BAMS-D-14-00173.1.

Torn, R. D., and G. S. Romine, 2015: Sensitivity of central Oklahoma convection forecasts to upstream potential vorticity anomalies during two strongly forced cases during MPEX. *Mon. Wea. Rev.*, **143**, 4064–4087, https://doi.org/10.1175/MWR-D-15-0085.1.

——, ——, and T. J. Galarneau Jr., 2017: Sensitivity of dryline convection forecasts to upstream forecast errors for two weakly forced MPEX cases. *Mon. Wea. Rev.*, **145**, 1831–1852, https://doi.org/10.1175/MWR-D-16-0457.1.

Trier, S. B., G. S. Romine, D. A. Ahijevych, R. A. Sobash, and M. B. Chasteen, 2021: Relationship of convection initiation and subsequent storm strength to ensemble simulated environmental conditions during IOP3b of VORTEX Southeast 2017. *Mon. Wea. Rev.*, **149**, 3265–3287, https://doi.org/10.1175/MWR-D-21-0111.1.

Wheatley, D. M., K. H. Knopfmeier, T. A. Jones, and G. J. Creager, 2015: Storm-scale data assimilation and ensemble forecasting with the NSSL Experimental Warn-on-Forecast System. Part I: Radar data experiments. *Wea. Forecasting*, **30**, 1795–1817, https://doi.org/10.1175/WAF-D-15-0043.1.

WSEC, 2006: A recommendation for an Enhanced Fujita scale (EF-scale). Texas Tech University Wind Science and Engineering Center Rep., 111 pp., https://www.depts.ttu.edu/nwi/Pubs/FScale/EFScale.pdf.

Yussouf, N., D. C. Dowell, L. J. Wicker, K. H. Knopfmeier, and D. M. Wheatley, 2015: Storm-scale data assimilation and ensemble forecasts for the 27 April 2011 severe weather outbreak in Alabama. *Mon. Wea. Rev.*, **143**, 3044–3066, https://doi.org/10.1175/MWR-D-14-00268.1.

——, T. A. Jones, and P. S. Skinner, 2020: Probabilistic high-impact rainfall forecasts from landfalling tropical cyclones using Warn-on-Forecast System. *Quart. J. Roy. Meteor. Soc.*, **146**, 2050–2065, https://doi.org/10.1002/qj.3779.